Proposal for the J-PARC 30-GeV Proton Synchrotron

Spectroscopy of Omega Baryons

K. Aoki[a], Y. Hidaka[b,c,d], A. Hosaka[e,f,g], N. Ishii[e], T. Ishikawa[h], Y. Komatsu[a], M. Naruki[i,f], H. Noumi[e,a], H. Ohnishi[h], K. Ozawa[a], Y. Morino[a], F. Sakuma[j], T. Sekihara[k], S.-I. Shim[l], K. Shirotori[e*], H. Takahashi[a], S. Takeuchi[m,g], and M. Takizawa[n,b,j]

[a] *Institute of Particle and Nuclear Studies (IPNS), High Energy Accelerator Research Organization (KEK), Tsukuba, Ibaraki 305-0801, Japan*

[b] *J-PARC Branch, Theory Center, Institute of Particle and Nuclear Studies (IPNS), High Energy Accelerator Research Organization (KEK), Tsukuba, Ibaraki 305-0801, Japan*

[c] *RIKEN iTHEMS, RIKEN, Wako 351-0198, Japan*

[d] *Graduate University for Advanced Studies (Sokendai), Tsukuba 305-0801, Japan*

[e] *Research Center for Nuclear Physics (RCNP), Osaka University, Ibaraki, Osaka 567-0047, Japan*

[f] *Advanced Science Research Center, Japan Atomic Energy Agency, Tokai 319-1195, Japan*

[g] *Nishina Center for Accelerator-Based Science, RIKEN, Wako 351-0198, Japan*

[h] *Research Center for Electron Photon Science (ELPH), Tohoku University, Sendai 982-0826, Japan*

[i] *Graduate School of Science, Kyoto University, Kyoto 606-8502, Japan*

[j] *RIKEN Cluster for Pioneering Research, RIKEN, Wako, Saitama 351-0198, Japan*

[k] *Graduate School of Life and Environmental Science, Kyoto Prefectural University, Kyoto 606-8522, Japan*

[l] *Department of Physics, Osaka City University, Osaka 558-8585, Japan*

[m] *Japan College of Social Work, Kiyose, Tokyo 204-8555, Japan*

[n] *Showa Pharmaceutical University, Machida, Tokyo 194-8543, Japan*

ver. June 14, 2021

*Spokesperson, E-mail: sirotori@rcnp.osaka-u.ac.jp

Executive summary of the proposed experiment

We propose the experiment to study Ω baryons at the K10 beam line of the extended Hadron facility. The Ω baryon is a unique but simple system which consists of three strange quarks. It would be the best place to study the internal structure of baryons, for example the origin of LS splitting, and the flavor symmetry for a variety of Roper-like resonances. The K10 is quite a beam line to provide us a high-intensity high-momentum negative kaon beam with high purity in the momentum region up to 10 GeV/c. We measure the masses, widths and decays of excited Ω baryons (Ω^*s) with excitation energies up to 1 GeV.

Beam line:	K10
Primary beam:	30 GeV, 50 kW at T2 target (5.2-s spill interval)
Secondary beam:	7, 8, 9, and 10 GeV/c K^-
Beam intensity:	7.0×10^6/spill on target
Reaction:	K^+K^{*0} and K^+K^0 production in the K^-p reaction
Detectors:	K10 spectrometer
Target:	Liquid hydrogen with a thickness of 57 cm
Beam time:	100 days for the physics run at 8 GeV/c, 10 days for the physics run at each of 7, 9, 10 GeV/c, and 10 days for commissioning
Estimated yield:	3.3×10^5 for each $\Omega^{(*)}$ in K^+K^{*0} production 4.6×10^6 for each $\Omega^{(*)}$ in K^+K^0 production

Contents

1 Physics background **4**

2 Spectroscopy of Ω baryons **6**
2.1 Spin dependent interactions 7
2.2 $1P$ states – quark orbital excitation 8
2.3 $1P$ states – moleculars 10
2.4 $2S$ states, physics of the Roper-like states 10

3 Conceptual design for the K10 beam line **12**

4 Experiment **18**
4.1 Spectrometer 18
4.1.1 Requirements for observing Ω^*s 19
4.1.2 E50 spectrometer 19
4.2 Performance of the spectrometer for observing Ω^*s 22
4.2.1 Acceptance of the $\Omega^{(*)}$-produced events 22
4.2.2 $\Omega^{(*)}$-mass resolution 24
4.2.3 Yield of the Ω^*-produced events 25
4.3 Expected $\Omega^{(*)}$ mass spectrum 27
4.3.1 Spectrum for signal contributions 27
4.3.2 Spectrum for background contributions 29
4.3.3 Spectrum for the sum of signal and background contributions . 30
4.3.4 Possible background reduction 30
4.3.5 Different incident kaon momenta 37
4.4 Decay angular distribution 38

5 Summary **41**

A Baryon spectroscopy with heavy flavors **43**
A.1 Baryon with a single heavy quark and two-light quarks 43
A.2 Baryon with a single heavy quarks with two-strange quarks 44
A.3 Determination of spin and parity 46

B ΩN scattering **48**
B.1 Introduction 48
B.2 Production of the ΩN bound state 48
B.3 Requirements for the spectrometer 49
B.4 Yield for the ΩN bound state 50
B.5 Mass resolution for the ΩN bound state 52

C ES-separator option for K10 beamline **56**

1 Physics background

Hadrons are composite particles of quarks interacting with gluons. Hence the goal of hadron physics is to answer the question "how quarks build hadrons". By this we should be able to explain various properties of observed hadrons, to predict new ones, and to tell how best to look for. The resulting knowledge can be used as the basis of various extended studies where hadrons appear such as dense hadronic matter. Furthermore, QCD is the only gauge theory that shows non-perturbative nature of dynamics and can be accessible by experiments. Thus the exploring QCD should be helpful to the understanding of what happens in various other physics systems, which can be described by the quantum field theories with the strong couplings.

Hadron spectroscopy has been studied for many years, mostly driven by experimental discoveries of new states [1]. Recent lattice QCD has been making crucial contributions to establish that QCD is indeed the theory of the strong interaction for hadrons, and opened a way even to nuclear systems from QCD. Nevertheless, there are still unsolved or unsettled problems in hadron spectroscopy. We tackle this issue of this project.

Let us start with looking at a simple example of atoms that are built by electrons (and a nucleus). An obvious fact is that the mass of the electron is much larger than the energies that are relevant to various atomic phenomena, the binding energies and excitation energies of electrons. Thus the creation of electron and anti-electron (positron) pair is suppressed, and therefore, the electrons inside an atom are essentially the same as isolated electrons, enabling the electrons as good building blocks, an "ordinary path" of how electrons build atoms. A similar situation occurs in nuclear systems.

The situation changes drastically for hadrons. Indeed the current u, d quarks in the QCD Lagrangian are far lighter than the proton [1]. This makes it very difficult to draw an ordinary path with the current quarks used as good building blocks. If we want to create the mass of the proton about 940 MeV from the current u, d-quark masses of order a few MeV, we need additional steps of many $q\bar{q}$ creations. Obviously such a process leads to enormous complications. If so is the resulting hadron spectrum so chaotic? In fact, the data seems very systematic in the region of excitation energies up to around 1 GeV, as shown in Fig. 1. This implies the emergence of effective degrees of freedom that build the observed hadrons in the ordinary sense.

This is the place where the non-perturbative dynamics of QCD comes in. A possible scenario is as follows. QCD is the SU(3) color gauge theory of quarks and gluons. The group structure of the theory necessitates the emergence of instantons in the vacuum; the QCD vacuum is no longer trivial. It is also a key element to solve the so-called $U_A(1)$ anomaly, a well-known example of which is the η-η' mass difference [3]. Then the instantons couple the left and right chirality components of light u, d, s quarks, leading to the three-body interaction of the u, d, s quarks, the instanton induced interaction

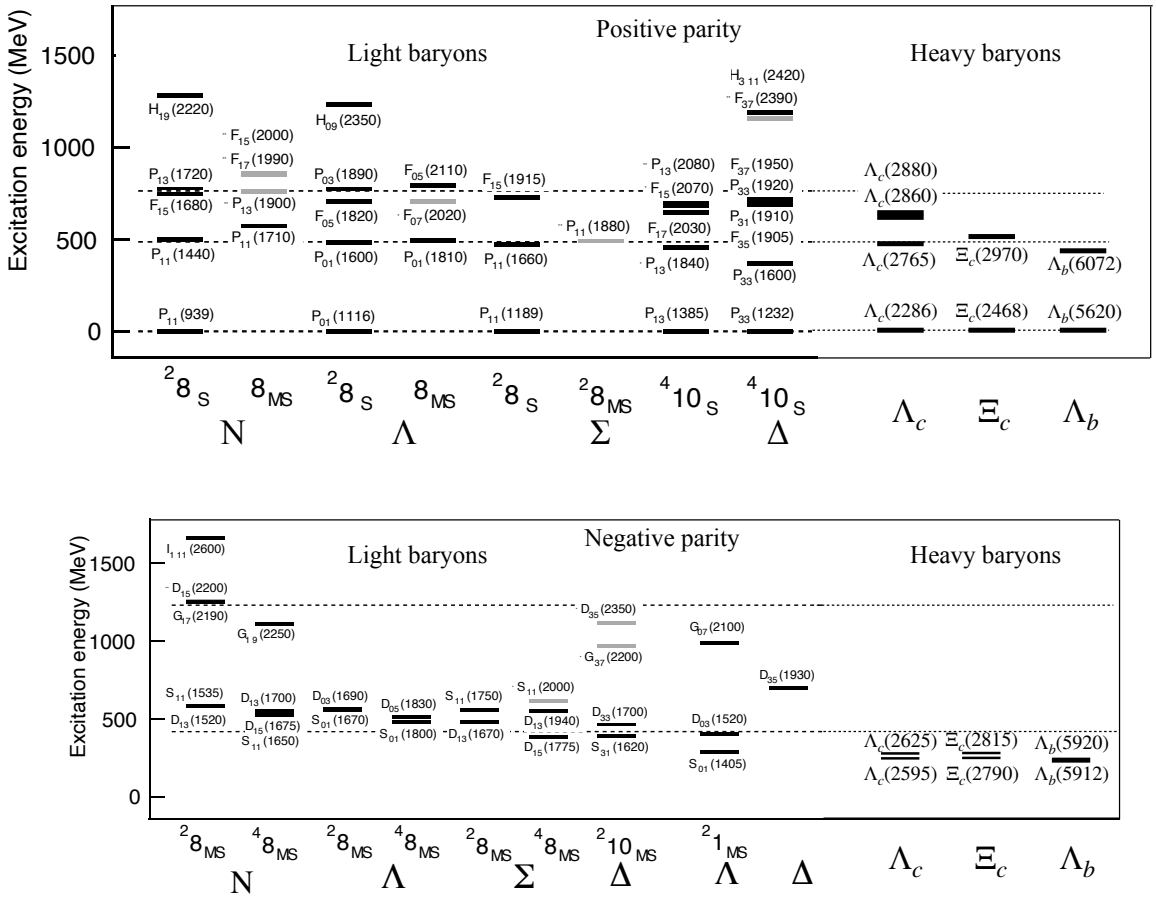

Figure 1: Excitation energies of various baryon states. Plots for u, d, s flavors are from ref. [2], with heavy baryon data are added.

(III). It takes the well-known form of determinant in the flavor space ($\det_{st}$) [4, 5]:

$$L_{\rm III} \sim \det_{st} \bar{\psi}^s (1+\gamma_5) \psi^t \tag{1}$$

It is shown that III causes the spontaneous symmetry breaking (SSB) of chiral symmetry that dresses the current quarks giving them finite masses, the emergence of constituent quarks. At the same time chiral symmetry requires the presence of the Nambu-Goldstone bosons, those are the pions. The constituent quarks and pions (mesons) are used as building blocks of hadrons. For baryon structure the constituent quarks are confined in the "quark core" region < 1 fm, and the pion forms the "meson cloud" around it, as sketched in Fig. 2. The gluons may also exist in the "quark core" region and interact weakly. If we consider higher excited states and the average inter-quark distance becomes large, then, the confinement force plays a sufficient role. It was shown that the theory naturally have a cutoff $\Lambda_\chi \sim 4\pi f_\pi \sim 1$ GeV, where f_π is the pion decay constant [6]. This is consistent with a typical instanton size ~ 0.2 fm, and also with the upper bound of the energy region where hadron resonances are

prominent.

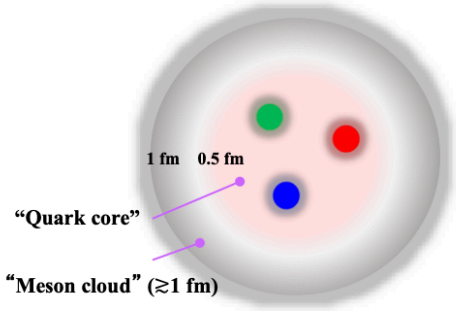

Figure 2: An intuitive view of baryon structure in terms of constituent quarks inside the "quark core" region and "meson cloud" around it.

To summarize we have an effective theory of quarks and pions. Quarks interact through the residual gluons, instantons and also pions. This setup of the effective theory follows the idea of the well known chiral quark model of Manohar-Georgi and can be the basis of the constituent quark model [6].

Parameters in the effective theory can be determined by comparing matrix elements containing the parameters in the effective theory that can be compared with one or few corresponding matrix elements which are conveniently computed by QCD, e.g., by lattice QCD. This is the idea of the matching of the effective theory. Once parameters are fixed an advantage of the effective theory is in its wide applicability to various phenomena, with keeping the link with QCD.

Our purpose is to explain observed phenomena consistently from the light to heavy flavored hadrons. The strategy is to measure and to utilize high quality data, and to analyze them by the effective theory based on QCD.

2 Spectroscopy of Ω baryons

The Ω baryon is a system of three strange quarks, sss. In flavor SU(3) symmetry it is assigned as a member of the decuplet representation, which was realized by the quark model whose building blocks are the u, d and s quarks. Here in what follows, these quarks are the "constituent" ones as we discussed in the previous section. Historically nine short-lived baryons of the spin $3/2^+$ were known, four Δ's, three Σ^*'s and two Ξ's fitting into the decuplet members, and the last piece Ω was predicted in the quark model [7]. The confirmation of Ω^- particle in 1973 [8, 9] supported the validity of the quark model based on the SU(3) flavor symmetry.

In reality, the SU(3) symmetry is broken by the mass of the s quark, which is heavier than the almost equal masses of u, d quarks. The pattern of SU(3) breaking could predict the mass of Ω under the equal mass spacing between the decuplet members.

The broken SU(3) also leads to the obvious mass difference of the pion ($m_\pi \sim 140$ MeV) and kaon ($m_K \sim 500$ MeV). This difference together with the singly flavored nature leads to the unique features of the Ω baryons.

First the sss combination put some restrictions on the wave function due to the Pauli's exclusion principle. For example, the fact that spin of the ground state Ω is 3/2 rather than 1/2 is precisely from that requirement. Similar restrictions apply to excited states. Some consequences from the restrictions may manifest in the fine structures of excited states. This will be discussed in Section 2.2.

Second is associated with the heavier mass of the kaon than that of the pion. In fact, the pion is very light as it is the NG boson, and therefore, it in many cases plays a role of radiation like a photon with the axial-vector nature. On the other hand, the kaon when coupled to excited states, it plays not only a role of radiation but also a role of a constituent forming hadronic molecule. This could be the reason that the $\Lambda(1405)$ can develop the molecular structure of $\bar{K}N$. A similar situation may occur in excited states of Ω's, which is also the subject in Section 2.3.

Third, the Ω baryons do not couple to the pion due to isospin symmetry. Therefore, without the meson cloud which exists in the light baryon structure, we may be able to directly access to the quark core region of the baryons. Furthermore, we may expect that an Ω baryon is smaller in spatial extension as compared to the light flavored baryons which is surrounded by meson cloud. We will discuss a related topic in Section 2.4

In the following we would like to discuss several unsolved/unsettled issues in hadron physics. To solve these problems, we consider it very important to approach the problems from various directions. High-intensity high-momentum negative kaon beams with high purity will contribute to it by the study of Ω baryon spectroscopy.

2.1 Spin dependent interactions

One of the longstanding mysteries in hadron physics is in the (hyper-)fine structure of spectrum associated with the spin-spin (ss) and spin-orbit (LS) interaction. The difficulty in the spin-spin interaction has been in the attempt to explain the decuplet-octet mass difference such as $N\Delta$ mass splitting, $\Delta M = M_\Delta - M_N \sim 300$ MeV. Having the "ordinary path", one would expect the one-gluon exchange (OGE) force between the constituent quarks as one possible source of the splitting. But then one need to set too large a coupling constant $\alpha_S > 1$, and if so perturbation calculation is no longer available.

The difficulty in the spin-orbit interaction is in the almost degenerate LS multiplets such as $S_{11}(1535)$ and $D_{13}(1520)$ — denoted by $N(1535)1/2^-$ and $N(1520)3/2^-$, respectively, in Review of Particle Physics [1]. Here the notation is $L_{2I\,2J}$ where L is the orbital angular momentum of the scattering pseudoscalar meson and baryon which form the resonant state, I is the isospin and J is the total angular momentum (For hyperons with an integer I, the notation is $L_{I\,2J}$). The situation is similar in other

expected multiplets as shown in Fig. 1. However, the use of the LS interaction derived from the OGE leads to large splittings of order 100 MeV or more [10].

Let us look at the above situation in a little bit more detail. As in QED, the interaction mediated by OGE decomposes into Coulomb (color-electric), spin-spin (color-magnetic) and spin-orbit interaction terms (and further terms [†]) in the non-relativistic expansion for the interaction. The corresponding potentials are written for the color $\bar{3}$ quark pair (ij) [11],

$$\begin{aligned} V_{ij}^{\rm Coul}(r_{ij}) &= -\alpha_S^{\rm Coul}\frac{2}{3r_{ij}} \\ V_{ij}^{ss}(r_{ij}) &= \alpha_S^{ss}\frac{16\pi}{9m_im_j}\delta(r_{ij})\vec{s}_i\cdot\vec{s}_j \\ V_{ij}^{LS}(r_{ij}) &= \alpha_S^{LS}\frac{1}{3r_{ij}}\left(\frac{1}{m_i^2}+\frac{1}{m_j^2}+\frac{4}{m_im_j}\vec{L}_{ij}\cdot(\vec{s}_i+\vec{s}_j)\right) \end{aligned} \tag{2}$$

A single color coupling constant would have to determine the strengths of the three terms, $\alpha_S^{\rm Coul}=\alpha_S^{ss}=\alpha_S^{LS}$, but actually phenomenological fitting requires that they are different, e.g., $\alpha_S^{\rm Coul}\sim 0.6$, $\alpha_S^{ss}\sim 1.2$ and $\alpha_S^{LS}\sim 0.08$. The strength for the Coulomb part is qualitatively consistent with the running coupling constant $\alpha_S(Q)$ at $Q\sim 1$ GeV while the other two are considerably different from it. These values indicate the anticipated problems; the spin-spin interaction α_S^{ss} is too large, while the spin-orbit interaction is suppressed. It was argued that the instanton induced interaction (III) can help to fill the discrepancy. The III contributes to the spin-spin interaction with the same sign as that of the OGE. It was shown that when the strength of III was fixed to reproduce the η-η' mass difference, about 40 % of the phenomenological strength of α_S^{ss} was brought by III. The III also contributes to the spin-orbit interaction which is now with opposite sign to that of OGE. Using the above α_S values, with the 40 % of $\alpha_S^{ss}\sim 1.2$ added to $\alpha_S^{\rm Coul}\sim 0.6$, we would find $\alpha_S^{\rm Coul}-0.4\alpha_S^{ss}\sim 0.1$ which agree qualitatively with the phenomenologically determined value olorred$\alpha_S^{LS}\sim 0.08$.

The above examples are the evidences of the III interaction that may resolve the mystery in the fine structure of baryon spectrum. It is shown that the OGE and III depend differently on quark flavors. Therefore, systematic studies over the wide range of flavors including Ω baryons will solve the unsolved/unconfirmed issues.

2.2 $1P$ states – quark orbital excitation

The confined constituent quarks can be excited orbitally. The lowest excited state is expected to be in P-wave with an orbital angular momentum $L=1$. In the spin-flavor SU(6) classification they form the 70-dimensional representation that are decomposed into spin-flavor multiplets ${}^{2S+1}\mathbf{N} = {}^2 8, {}^2 10, {}^4 8$ and ${}^2 1$. Here S is the total intrinsic spin of the three quarks, $S=1/2, 3/2$, and $\mathbf{N}$ the dimension of the flavor representation.

[†]In addition to these terms, there are antisymmetric LS and tensor terms.

Among them, $^2 8$ and $^4 8$ are assigned to N, Λ, Σ and Ξ baryons, and $^2 1$ to $\Lambda(1405)$ and $\Lambda(1520)$. Then the $^2 10$ representation includes the P-wave Ω together with Δ, Σ and Ξ excited states. Because of their intrinsic spin $S = 1/2$, they form the spin doublet, $J = S + L = 1/2, 3/2$, and their parity is negative due to the P-wave. It is emphasized that in the standard picture, there must be $2S+1$ or $2L+1$ fold degeneracies depending on whether $S < L$ or $S > L$, respectively.

The $\Omega(2012)$ which has been recently reported from Belle is a candidate of one of the multiples [12]. The mass 2012 MeV is about 500 MeV above the expected ground state when possible spin-spin interaction contribution is removed. Therefore, the state is expected to be one of doublets of $^2 10$. Its decay width is as narrow as $6.4^{+2.5}_{-2.0} \pm 1.6$ MeV. The decay $\Omega(2012) \to \Xi \bar{K}$ was studied in the quark model, resulted in a decay width about 12 MeV for $J^P = 1/2^-$ and about 6 MeV for $J^P = 3/2^-$. The width of the $J^P = 3/2^-$ state is narrower due to its D-wave nature of the decaying two-body channel in the final state. Therefore, the quark model seems to prefer $3/2^-$ state.

Assuming a two-body LS interaction, we need both $L = 1$ and $S = 1$, where L and S are the orbital angular momentum and spin of an ss pair. However, such a combination is not allowed due to the Pauli principle, when spin, flavor, orbital and color wave functions are combined. Therefore, we expect that the LS splitting of $1/2^-$ and $3/2^-$ is suppressed for these Ω states.

As anticipated the two-body spin-orbit interaction is derived from the OGE and III interactions. In many cases they contribute with opposite signs, while in others only the OGE survive due to flavor anti-symmetric nature of III and its suppression for heavy quarks systems. Such relations are summarized in Table 1 for various baryon states, where expectation not only for P-wave but also for D-wave excitations, where in the latter the OGE from the III may exclusively contribute to the Ω's. In Ref. [13], a phenomenological LS interaction was introduced resulting in significant splittings. One possible origin of such an interaction would be three-body nature. The clarification of the LS splitting is crucial to the systematic understanding for the baryon spectroscopy.

Table 1: Expected contributions of LS interaction to various baryons. In the second line P and D denote the orbital angular momentum of quarks inside baryons. Positive values A and B represent matrix elements of the LS interaction which depend on baryon states, and their computations were performed, for instance, in Ref. [10]. The symbol "?" indicates that there is no experimental data.

	Ω^*		N^*		Λ^*		Λ_c^*	
Orbit	P	D	P	D	P	D	P	D
OGE	–	$+A$	$+A$	$+A$	$+A$	$+A$	$+A$	$+A$
III	–	–	$-B$	$-B$	$-B$	$-B$	–	–
Sum	0	$+A$	~ 0	~ 0	small	small	$+A$	$+A$
Exp (MeV)	?	?	~ 0	~ 0	36	?	34	?

2.3 $1P$ states – moleculars

Another interpretation has been proposed for $\Omega(2012)$; since its mass is located approximately 10 MeV below the $\Xi^*\bar{K}$ threshold, it could be a $\Xi^*\bar{K}$ molecular state [14, 15]. The formation of such a molecular state is expected near the threshold region of two or more particles with some heavy mass. The Ξ^* and $\bar{K}$ would be such. Though the kaon is heavier than the pion, it also shares the properties of the NG boson when the chiral interaction is effective. In this regards, the system shows an interesting feature; the direct interaction for $\Xi^*\bar{K}$ is absent, but the offdiagonal interaction to the coupling to $\Omega\eta$ with higher mass can drive an attraction. The decay width was also estimated by chiral counting, expecting values consistent with the data [14]. The mechanism itself is interesting, and deserves study. A caveat in this picture is that $1/2^-$ state is not easy to be explained.

To establish the nature of $\Omega(2012)$ is an urgent issue in the present project. The determination of basic properties of such as spin and parity, decay width, and also a search of spin partner provides an important information to explore the Ω spectroscopy.

2.4 $2S$ states, physics of the Roper-like states

Baryon resonances possessing the same spin-parity as that of the ground states are of special interest. By now many such states are observed in a wide range of flavor contents; $N(1440)1/2^+$, $\Lambda(1600)1/2^+$, $\Sigma(1660)1/2^+$, $\Delta(1600)3/2^+$ and $\Xi_c(2970)1/2^+$. The nucleon resonance $N(1440)$ has been known for long time as the Roper resonance, while $\Xi_c(2970)$ has been established only recently [16]. Furthermore, $\Lambda_c(2765)$ and newly found $\Lambda_b(6072)$ [17, 18] are also expected to be their siblings. Interestingly all of their masses are about 500 MeV above their corresponding ground states as shown clearly in Fig. 1.

In the nucleon sector the problem has been known as too low mass of the Roper resonance. In the quark model the $1/2^+$ state is realized as a radial (nodal) excitation whose mass appears at around 1800 MeV which is obviously too high as compared to the observed one of 1440 MeV. Related to this the quark model predicts the wrong mass ordering; the Roper resonance appears higher than the negative parity state, for instance $N(1535)1/2^-$. A lowering mechanism has been proposed due to the meson cloud around the quark core of u, d quarks [19, 20]. Turning to the heavy quark sector, due to the lowering of the λ-mode, the observed states of positive and negative parities appear as in the expected order with their mass values qualitatively consistent with the quark model predictions. Thus another option to explain the equal excitation masses is flavor dependent mechanism so as to cancel the natural flavor dependence in the quark model. These two interpretations for the Roper resonance and siblings must be converged.

To answer this question, information of Ξ and Ω resonances are useful. The mass of the strange quark is between those of light and heavy quarks, and therefore more strange baryons interpolate the light and heavy flavor dynamics, filling the missing

link between the two. As anticipated, with the suppression of the meson cloud the Ω baryons provide an ideal platform to extract the dynamics of the constituent quarks. This is particularly expected in the study of various transitions such as radiative decays $\Omega^* \to \Omega\gamma$ and kaon decays $\Omega^* \to \Xi\bar{K}$ since the decay rates are sensitive to the forms of the wave functions.

The decay of the Roper-like state through one kaon emission $\Omega^* \to \Xi\bar{K}$ may contain interesting physics. The decay occurs by the chiral interaction between the NG kaon and quarks,

$$\mathcal{L}_{\phi qq} = \frac{g_A^q}{f_\pi}\ \bar{q}\gamma_\mu\gamma_5\lambda_a q\ \partial^\mu\phi^a \tag{3}$$

where ϕ^a is the flavor SU(3) NG boson field and $g_A^q \sim 1$ [21] the axial coupling constant of the quark. In the previous publications, the Lagrangian was expanded non-relativistically and took up to the first order in the velocity $v \sim p/m$ of the quarks where p is the momentum of a quark inside the baryon,

$$\mathcal{L}_{\pi qq} \sim\ \frac{g_A^q}{f_\pi}\left(\vec{\sigma}\cdot\vec{q} + \frac{\omega_\pi}{2m_q}(\vec{\sigma}\cdot\vec{q} - 2\vec{\sigma}\cdot\vec{p})\right) \tag{4}$$

The problem of the truncation up to this order is in the fact that the leading term of order v^0 vanishes exactly due to the operator structure of $\vec{\sigma}\cdot\vec{q}$ where $\vec{q}$ is the momentum carried by the kaon, and the orthogonality between the wave functions of the radially excited and ground states in the long wave length limit. Such a kind of forbidden process was originally pointed out in the radiative decay of the nucleon Roper resonance [22]. The next to leading order term of v^1 also turns out to be small. Actual computation shows that these terms (and similar studies) predicted only small decay widths which contradicts the observed data [23, 24].

Thus next-next to leading order term of v^2 is important. Explicitly

$$\mathcal{L} \sim \frac{g_A^q}{f_\pi}\left(\frac{m_\pi^2}{8m_q^2}\vec{\sigma}\cdot\vec{q} + \frac{1}{4m_q^2}\vec{\sigma}\cdot(\vec{q} - 2\vec{p})\times(\vec{q}\times\vec{p})\right) \tag{5}$$

The second term is the dominant term which results in the transition matrix element as proportional to $\langle p^2\rangle \sim 1/\langle r^2\rangle$, which survives in the long-wave length limit with no forbidden selection rule applies. Physically, we can interpret that the transition rate is dictated by the Fermi motion of the confined quarks and hence the inversely proportional to the size of the quark core of baryons. It was shown that such higher order term contributed significantly to the decay width of the heavy baryons and improved the agreement with the data [23]. A preliminary calculation show the decay width of the Roper-like Ω is around 100 MeV after the inclusion of the v^2 contributions, while the terms of order v^0 and v^1 give only around 20 MeV. The small value in the lower order terms is qualitatively consistent with the previous studies.

After discussing this much about the Roper-like Ω, it is very important to observe the state and to measure the width. The width is interesting in that it carries the information of the internal motion of constituent quarks in the core region which is related to the size of that region.

3 Conceptual design for the K10 beam line

High-intensity high-momentum negative kaon beam with high purity is a crucial ingredient for the proposed experiment. Therefore, the K10 beam line under discussion in the project "Hadron hall extension" is the only place where the proposed experiment can be performed.

Two options are under consideration for the particle separation at the K10 beam line; an ordinary electrostatic (ES)-separator option and an RF-separator option. The ES-separator option can be applied up to $4 \sim 6$ GeV/c. In contrast, the RF-separator option is suitable for higher momentum. By making a common design at the front-end section of both options of the beam line, we can switch the separation method without accessing the high-radiation area. The production angle of secondary beams is chosen to be 3 degrees, which is smaller than those of the K1.8 and K1.1 beam lines, because the production cross-sections of K^- and $\bar{p}$ at 3 degrees are about five times larger than those at 6 degrees, according to the empirical formula by Sanford and Wang [25]. Since the separation by an ordinary ES separator is proportional to $1/p^3$, the separation is much difficult for the momentum higher than 4 GeV/c (K^-) or 6 GeV/c ($\bar{p}$). Therefore, we need RF separators to handle such a high-momentum region, which is essential for the proposed experiment.

The principle of the particle separation by using RF cavities is schematically shown in Fig.3. In this method, two RF cavities (RF1 and RF2) are located in the beam line, and the optics between the two cavities are set so that the transport matrix is equal to "$-I$". If the RF amplitude of the two cavities are the same, the sum of the beam deflection from the two cavities is

$$D = -A\sin(\omega t) + A\sin(\omega t + \Delta\phi) \quad (6)$$

$$= 2A\sin\frac{\Delta\phi}{2}\cos\left(\omega t + \frac{\Delta\phi}{2}\right), \quad (7)$$

where ωt is the phase at the first cavity, and $\Delta\phi$ the phase difference between the two

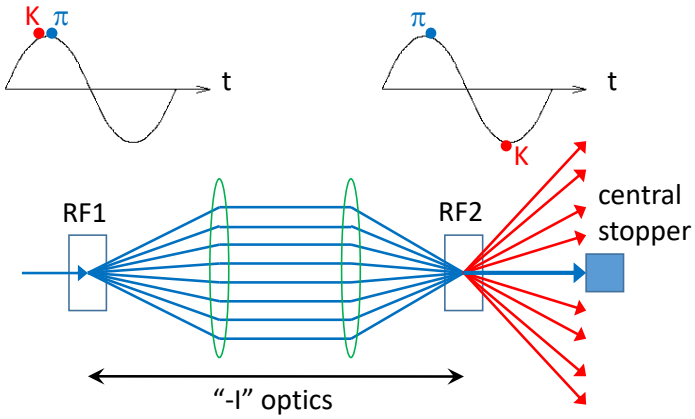

Figure 3: The principle of the particle separation using two RF cavities.

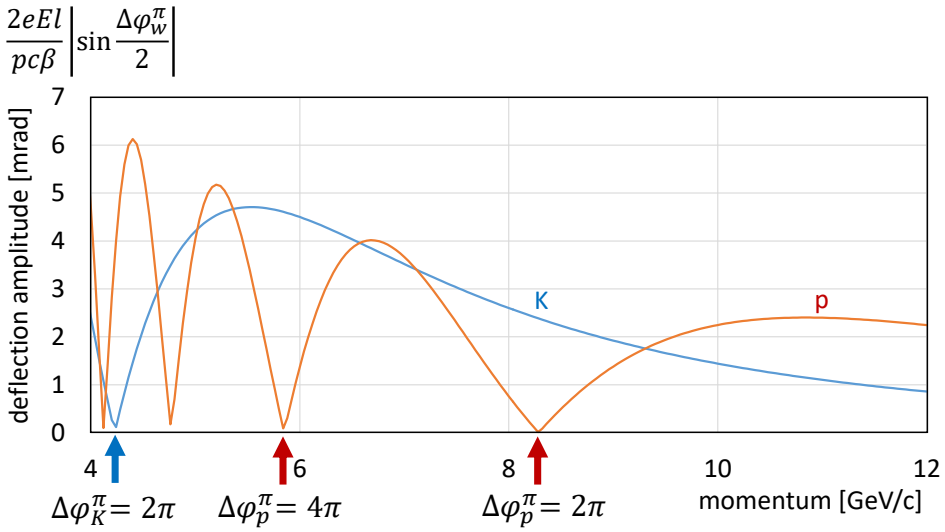

Figure 4: Momentum dependence of the deflection amplitude for K^- (blue) and $\bar{p}$ (red) in the case that the RF phase of the two cavities are same for π^-. Since the deflection for π^- is always canceled, usable is the momentum region in which the deflection for K^- or $\bar{p}$ is large.

cavities. The minus sign in the first line comes from the "$-I$" optics between the two cavities. The amplitude A is given by

$$A = \frac{eEl}{pc\beta}, \tag{8}$$

where e, p, and β are the charge, momentum, and velocity of the particle, respectively, and E and l denote the field gradient and the effective length of the cavity, respectively. When the phase at the second cavity is set to be same as that of the first cavity for an unwanted particle, namely π, the deflection of the particle is canceled in whichever phase it passes the first cavity, and it is absorbed with a central stopper downstream. On the other hand, the phase of the second cavity for particles with the other mass and velocity (K^- or $\bar{p}$) differs by

$$\Delta\phi_w^u = \frac{2\pi fL}{c}\left(\frac{1}{\beta_w} - \frac{1}{\beta_u}\right) \tag{9}$$

$$\sim \frac{\pi fL}{c}\frac{m_w^2 - m_u^2}{p^2c^2}, \tag{10}$$

they are deflected by $2A\sin\frac{\Delta\phi_w^u}{2}$ in maximum depending on the phase at the first cavity, and pass outside of the central stopper. Here, f is the RF frequency, L the distance between the two cavities, p the momentum, and β_w/β_u and m_w/m_u are the velocities and masses of the wanted/unwanted particles, respectively.

For example, assuming π^- as an unwanted particle, the momentum dependence of the deflection amplitude for K^- and $\bar{p}$ in the case of $f = 2.857$ GHz and $L = 16.8$ m

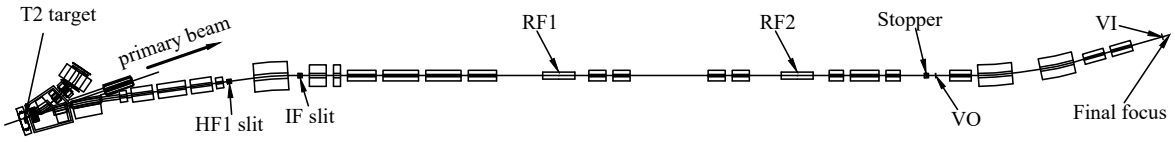

Figure 5: Layout of the RF option of the K10 beam line.

is plotted in Fig.4. The deflection for the wanted particle is also canceled in the momentum range corresponding to

$$\Delta\phi_w^u = 2n\pi \ \ (n = 1, 2, 3, ...), \tag{11}$$

whereas the deflection get maximum in the range satisfying

$$\Delta\phi_w^u = (2n-1)\pi \ \ (n = 1, 2, 3, ...). \tag{12}$$

Another operation mode can be considered where the phase of the second cavity is tuned to be same as that of the first cavity for a wanted particle (K^- or $\bar{p}$). Then the deflection of the wanted particle is always canceled, while the unwanted particle (π^-) is deflected depending on the phase difference and is eliminated with a slit.

The layout of the RF-separator option of the K10 beam line is presented in Fig.5, and the beam envelope calculated with the TRANSPORT code [26] is shown in Fig.6. The total length of the beam line is 80.7 $\sim$ 81.2 m depending on the configuration of the beam spectrometer. The RF frequency and the distance between the cavities are set to 2.857 GHz and 16.8 m, respectively. The effective length of the cavities is 2.25 m.

The beam line consists of three sections; the front-end section, the separation section, and the analyzing section. In the front-end section, secondary beams generated at the production target are extracted from the primary beam line, and focused vertically at the intermediate (IF) slit to reduce so-called "cloud π". The optics are also tuned to make beams almost achromatic at the IF slit. In the separation section, the optics is tuned to obtain a parallel and narrow beam at the RF cavity, and the transport matrix of "$-I$" is realized between the cavities by using four quadrupoles with same field gradient. After analyzed with a beam spectrometer, the beam is focused to an experimental target both in horizontal and vertical directions.

As for the beam spectrometer, we have two types of the configuration. Type I consists of two dipole magnets and three quadrupoles with the order of QDDQQ, as shown in Fig. 6. In the transport matrix of the section from VO to VI, the condition of the point-to-point focus is satisfied in the horizontal direction ($R_{12} = 0$), and the magnification (R_{11}) and the dispersion (R_{16}) are -1.627 and -0.635 cm/%, respectively. By assuming the position resolution of tracking devices located at VO and VI is $\sigma_x = 300$ μm, the expected momentum resolution is $\sigma_p = \frac{\sqrt{1+R_{11}^2}}{|R_{16}|}\sigma_x = 0.090$ %.

Another design, Type II, has a QQDDQ configuration (Fig. 7). It also realizes the point-to-point focus ($R_{12} = 0$) from VO to VI, and has the magnification of

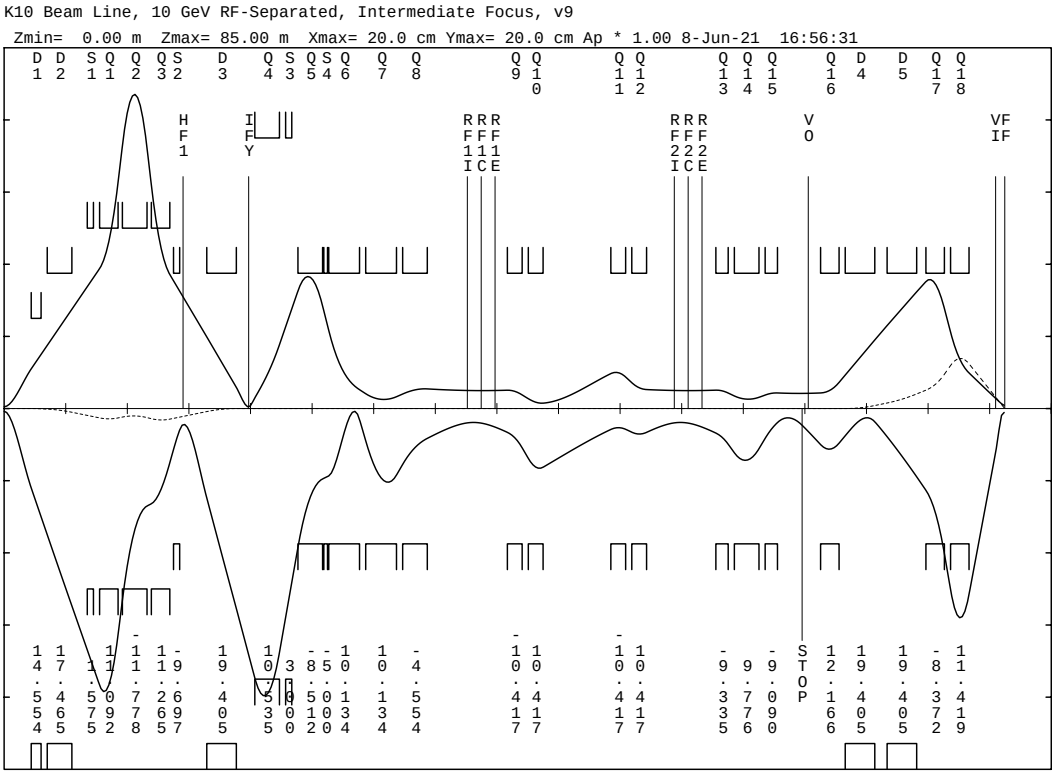

Figure 6: First-order beam envelope of the RF option of the K10 beam line. The upper and lower show the vertical and horizontal directions, respectively. The dash line indicate the horizontal dispersion.

$R_{11} = -0.228$ and the dispersion of $R_{16} = -0.354$ cm/%. The expected momentum resolution, therefore, is 0.087 %.

Compared with Type II, the vertical beam size in the analysing section in Type I is so large that it causes a transmission problem when the phase of the second cavity is tuned to π^-'s (π-tuned mode). Type I spectrometer, therefore, can be used only with a slit in a K-tuned or a $\bar{p}$-tuned mode. On the other hand, Type II can be operated with a central stopper in a π-tuned mode as well as a slit in a K- or $\bar{p}$-tuned mode.

Table 2 lists the result of the beam simulation using DecayTURTLE [27] for each type of the beam spectrometer and the operation mode, assuming the beam loss of 25 kW at the production target and the spill repetition of 5.2 s. The horizontal and vertical beam profiles are shown in Fig. 8. Type II has an advantage in terms of intensity and purity, whereas Type I provides a much smaller beam spot size at the experimental target.

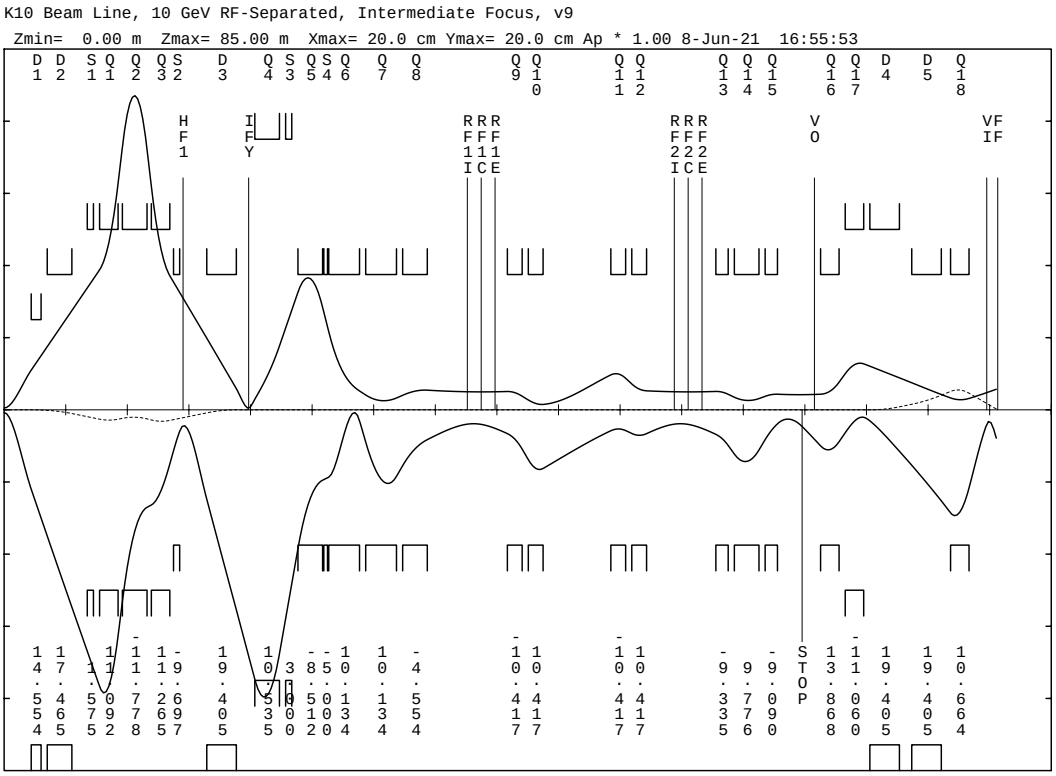

Figure 7: Same as Fig.6 but for Type II of the beam spectrometer.

Table 2: Expected K^- intensity per spill and purity (K^-:π^-) of the RF option of the K10 beam line. The beam loss of 25 kW at the production target and the spill repetition of 5.2 s were assumed. The production cross-section was calculated by using Sanford and Wang formula. Decay muons and so-called "cloud-π" were not included. Slit conditions were varied to achieve a moderate purity for each case. The field gradient of RF cavities was also varied in the range from 5 to 9 MV/m.

	Type I (QDDQQ) K-tuned mode	Type II (QQDDQ) π-tuned mode	Type II (QQDDQ) K-tuned mode
5 GeV/c	3.9×10^6 (1:7.0)	5.4×10^6 (1:3.5)	6.1×10^6 (1:7.8)
6 GeV/c	5.2×10^6 (1:5.0)	7.3×10^6 (1:2.6)	8.4×10^6 (1:5.4)
7 GeV/c	6.0×10^6 (1:4.8)	8.3×10^6 (1:2.1)	9.4×10^6 (1:5.1)
8 GeV/c	5.8×10^6 (1:5.7)	7.9×10^6 (1:2.1)	9.1×10^6 (1:6.1)
9 GeV/c	4.9×10^6 (1:7.3)	6.7×10^6 (1:2.1)	8.0×10^6 (1:7.6)
10 GeV/c	4.0×10^6 (1:9.4)	4.7×10^6 (1:2.5)	6.4×10^6 (1:10.0)

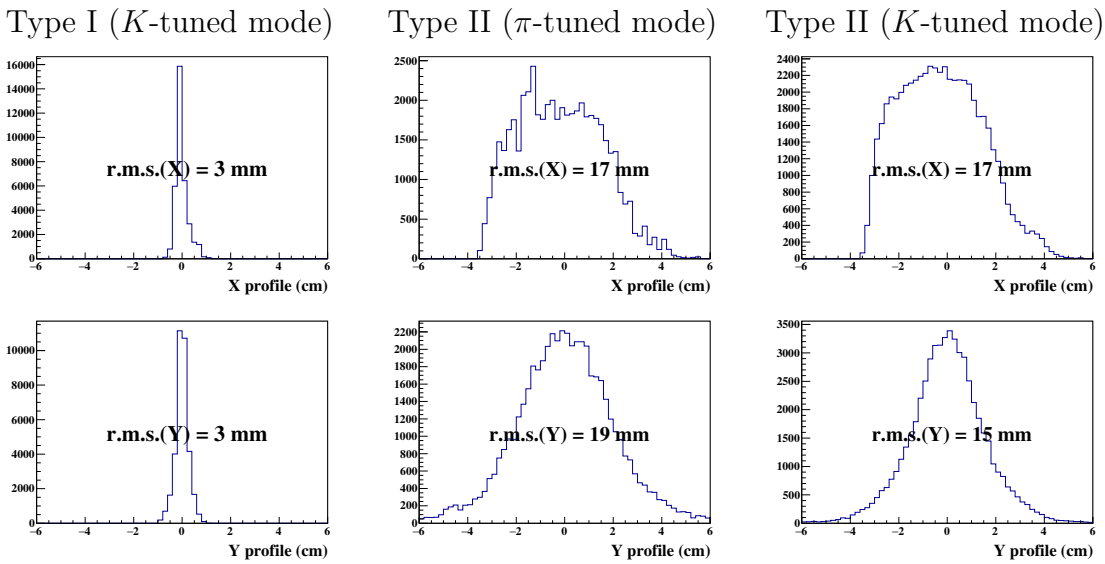

Figure 8: Expected beam profile at the final focusing point for each type of the beam spectrometer and the operation mode.

4 Experiment

We plan to study the masses and decays of excited Ω baryons (Ω^*s) in the $K^-\ p \to \Omega^{*-}\ K^+\ K^{*0}$ and $K^-\ p \to \Omega^{*-}\ K^+\ K^0$ reactions at incident kaon momenta ranging from 7 to 10 GeV/c. Figure 9 shows the schematic view of the production mechanisms of Ω^*s in the K^-p reaction, and their decay. The mass of a produced Ω^* including the ground-state Ω ($\Omega^{(*)}$) can be determined in a missing-mass technique using the four-momenta of the initial-state $K^-\ p$ and final-state $K^+\ K^+\ \pi^-$ ($K^+\ \pi^+\ \pi^-$) in the $K^-\ p \to \Omega^{(*)-}\ K^+\ K^{*0}$ ($K^-\ p \to \Omega^{(*)-}\ K^+\ K^0$) reaction. Here, the selected events are those in which the $K^+\ \pi^-$ ($\pi^+\ \pi^-$) invariant mass should give the K^{*0} (K^0 or K_S) mass. Since the four-momentum of the produced Ω^* is already given in the missing-mass technique, the dominant decay mode $\Omega^{*-} \to \Xi^0\ K^-$ ($\Omega^{*-} \to \Omega^-\ \pi^+\ \pi^-$) can be identified only by detecting the emitted K^- ($\pi^+\ \pi^-$) and calculating the mass of the daughter Ξ^0 (Ω^-) particle in a similar missing-mass technique. Both the production and decay measurement of Ω^*s are essential in their systematic studies.

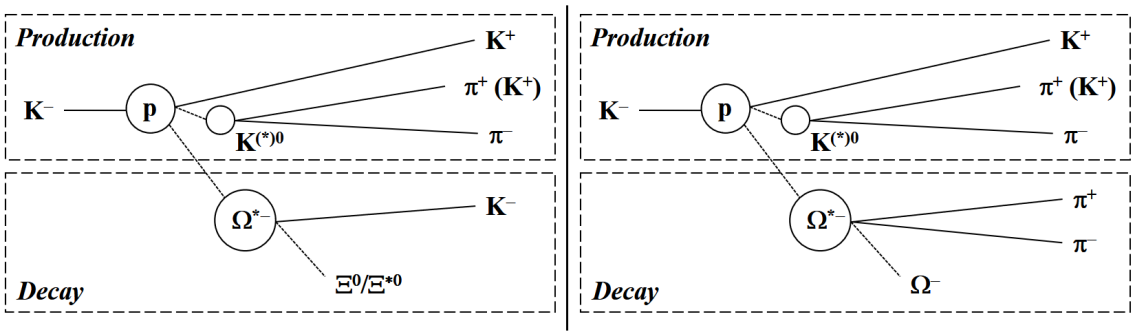

Figure 9: Schematic view of the production mechanisms of Ω^*s in the $K^-\ p$ reaction, and their decay. The solid lines represent the initial- and final-state particles to be directly detected. The dashed lines show unstable particles to be reconstructed from kinematic variables of the detected particles. Ω^*s are expected to decay into $\Xi^0\ K^-$ (left) and $\Omega^-\ \pi^+\ \pi^-$ (right).

4.1 Spectrometer

High-intensity high-momentum K^- beam is necessary to produce $\Omega^{(*)}$s effectively. At such incident kaon momenta producing Ω^*s, high-momentum particles are likely to be emitted at forward angles in the laboratory frame when we use a stationary target. A spectrometer system with a dipole magnet covering the forward direction is suitable to detect these particles to get high mass-resolution for Ω^*s. In this subsection, we discuss the requirements for the spectrometer in Ω baryon spectroscopy and show a possible candidate of the spectrometer at the K10 beam line.

4.1.1 Requirements for observing Ω^*s

In Ω baryon spectroscopy, we have to primarily measure the excitation spectrum of $\Omega^{(*)}$s, and determine the angular distribution of a daughter particle from their decay. $\Omega^{(*)}$s are produced in the $K^-\ p \to \Omega^{(*)-}\ K^+\ K^{*0}$ and $K^-\ p \to \Omega^{(*)-}\ K^+\ K^0$ reactions at incident kaon momenta ranging from 7 to 10 GeV/c. Since the $\Omega^{(*)}$-produced events are identified by the $p(K^-, K^+K^{*0})$ and $p(K^-, K^+K^0)$ missing mass[‡] with the $K^{*0} \to K^+\ \pi^-$ and $K^0 \to \pi^+\ \pi^-$ decays, high acceptance is required for detecting the final-state $K^+\ K^+\ \pi^-$ and $K^+\ \pi^+\ \pi^-$ particles. Additionally, high momentum resolution is necessary for each of them to get enough high Ω^*-mass resolution (2.5–4.5 MeV in σ) for observing Ω^*s separately, and determining their width directly from the mass spectrum. The daughter particles from the Ω^* decays should be detected in a wide angular coverage for determining the spin-parity of an Ω^*. The requirements for the spectrometer system are as follows:

- wide angular coverage of polar angles up to 30° for detecting the final-state $K^+\ K^+\ \pi^-$ and $K^+\ \pi^+\ \pi^-$ particles,
- wide angular coverage of polar angles up to 45° for detecting the daughter particles from the Ω^* decays,
- high momentum-resolution of a few 10^{-3} (σ)
- multi-layer tracking system to detect multiple particles, and
- high particle-identification power, the efficiency is higher than 97%, and mis-identification fraction is lower than 1% for 0.2−8.0 GeV/c particles.

4.1.2 E50 spectrometer

A spectrometer satisfies these requirements to be constructed for the charmed baryon spectroscopy experiment (J-PARC E50 [28]). Figure 10 shows the schematic view of the E50 spectrometer. In the E50 experiment, the charmed baryons Y_c^{*+} are produced in the $\pi^-\ p \to Y_c^{*+}\ D^{*-}$ reaction. Similarly to the proposed experiment for Ω baryon spectroscopy described in this proposal, the Y_c^{*+} mass is determined in the E50 experiment from the $p(\pi^-, D^{*-})$ missing mass by detecting the final-sate $K^+\ \pi^-\ \pi^-$ particles from the D^{*-} decay. The daughter particles from the Y_c^{*+} decay are also planned to be detected. The E50 spectrometer is designed for detecting all the charged particles produced in the $\pi^-\ p \to Y_c^{*+}\ D^{*-}$ reaction at an incident pion momentum of 20 GeV/c. Emitted at forward angles are high-momentum particles from the $D^{*-} \to \bar{D}^0\pi^-$ decay

[‡]The reaction of interest is often denoted by $T(I,S)R$ for scattering experiments in Nuclear Physics, where I, T, S, and R stand for the incident, target, scattering, and recoil particles, respectively. We use this notation also in Hadron Physics by using S for a set of detected particles, and R a set of undetected particles. When R is comprised of a single particle, its mass can be calculated from four-momenta p of I, T, and S: $m_R^2 = p_R^2 = (p_I + p_T - p_S)^2$. We call m_R the $T(I,S)$ missing mass.

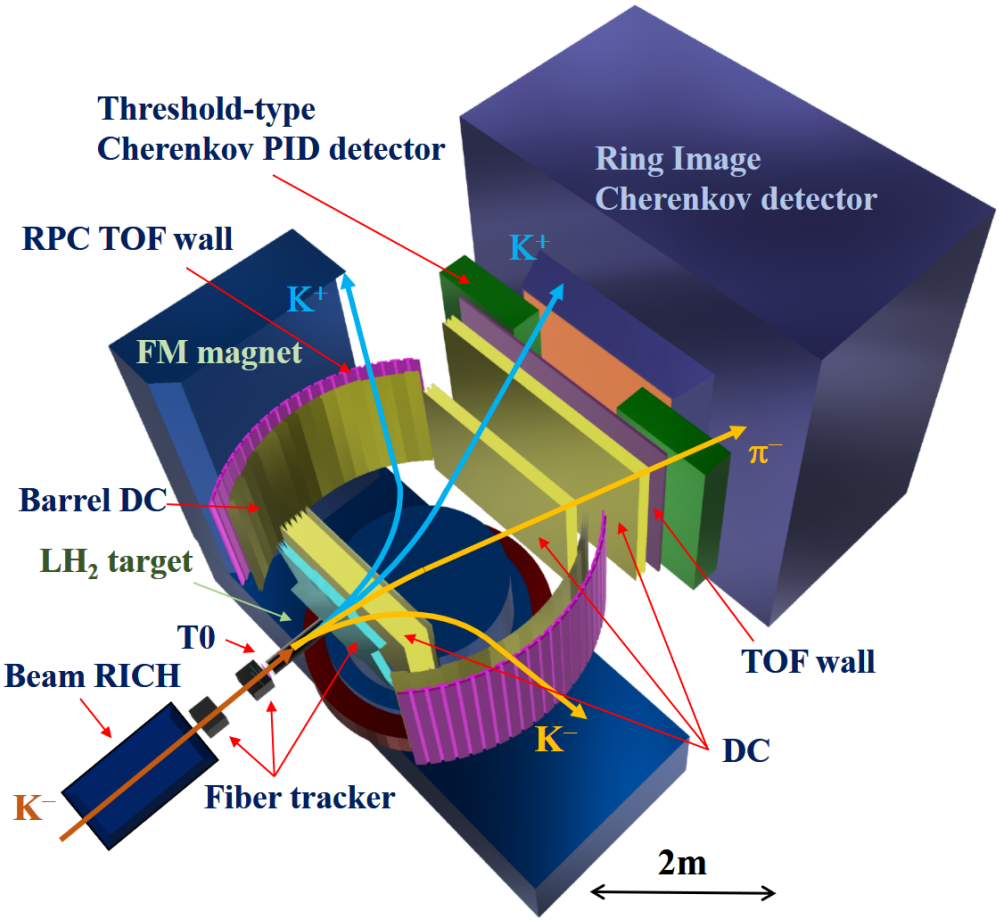

Figure 10: Schematic view of the spectrometer to be constructed for the E50 experiment at J-PARC. It consists of a large dipole magnet, tracking detectors, time-of-flight detectors, and particle-identification detectors. Some of tracking detectors and time-of-flight detectors are placed inside the gap of the magnet (internal detectors).

followed by $\bar{D}^0 \to K^+ \pi^-$ as well as daughter particles from the Y_c^{*+} decay. The momentum of the emitted particles ranges from 0.2 to 16 GeV/c. The stationary target is placed just in front of the entrance of the dipole magnet. The details of the E50 spectrometer are described elsewhere [29]. The E50 spectrometer is designed as a multi-purpose system at the high-momentum beam line, and it can be used also in the proposed experiment for Ω baryon spectroscopy.

The E50 spectrometer consists of a large dipole magnet, tracking detectors, time-of-flight detectors, and particle-identification detectors. To determine the Y_c^{*+} mass from the $p(\pi^-, D^{*-})$ missing mass, it is necessary to measure the four-momentum of the final-sate K^+ π^- π^- particles. Since high-momentum K^+ and π^- from the $\bar{D}^0$ decay are emitted at forward angles, placed at forward angles are scintillating-

fiber hodoscopes [30] behind the target, several drift chambers (DCs), and ring-image Cherenkov detector (RICH) for the trajectory determination (momentum analysis), time-of-flight (TOF) measurement, and particle identification, respectively. Additional tracking and time-of-flight detectors are placed inside the gap of the magnet (internal detectors) to detect the slow π^-s emitted at forward angles from the D^{*-} decay (not from the $\bar{D}^0$ decay) and daughter particles from the Y_c^{*+} decay. These detectors should have a wide angular coverage since the slow π^-s cannot reach the exit of the dipole magnet and since the daughter particles are emitted in a wide angle range. Placed in front of the magnet yokes are the barrel-shaped DCs and high time-resolution TOF detector wall consisting of resistive-plate chambers (PRCs) for detecting the slow π^- and horizontally-emitted Y_c^{*+} daughter particles. The RPCs are also placed on the pole pieces for detecting vertically-emitted Y_c^{*+}. The scintillating-fiber hodoscopes and DCs located behind the target are used not only for high-momentum $K^+\pi^-$ particles at forward angles but also for all the produced particles. To get high-counting rate capability, the scintillating-fiber hodoscopes are planned to be used just behind the target. They are also placed at upstream of the target for measuring the incident momentum and profile, or (x, y) intensity map. To get the reference timing for all the detectors, the fine-segmented acrylic Cherenkov counter (time-zero counter) [31] is placed just in front of the target. Another RICH counter, Beam RICH [32], is used for identifying incident particles in the secondary beam located at most upstream.

We plan to use a trigger-less streaming data acquisition (DAQ) system [33, 34] in the experiment for Ω baryon spectroscopy. This DAQ system selects the events corresponding to the reaction of interest without any hardware trigger (trigger-less). All the detector signals are digitized in front-end electronics, and the digitized data fragments are continuously transfered (streaming) to a personal computers (PCs). The events of interest are selected using software on PCs by combining the streaming data fragments. In a streaming DAQ, a complicated hardware trigger system is not necessary, which makes a busy time for processing an event corresponding to a trigger. We are developing this streaming DAQ system for the E50 experiment as well as a special time-to-digital converter (TDC) for a continuous time measurement without any external trigger. We have tested and successfully demonstrated a prototype DAQ system [33,34] using high-intensity electrons and positrons converted from a bremsstrahlung photon beam at the Research Center for Electron Photon Science, Tohoku University [35]. The streaming DAQ system allows us to make the DAQ efficiency close to 100% without any trigger bias.

Before performing Ω baryon spectroscopy at the K10 beam line, we need some pilot experiments at the existing high-momentum beam line for measuring cross sections for the elementary processes of multi-strangeness production and studying excited states of hyperons. Although the E50 spectrometer satisfies the proposed experiment at the K10 beam line, a new spectrometer dedicated to Ω baryon spectroscopy as well as studies of the low-energy ΩN scattering described in section B is desired to be construed at the K10 beam line.

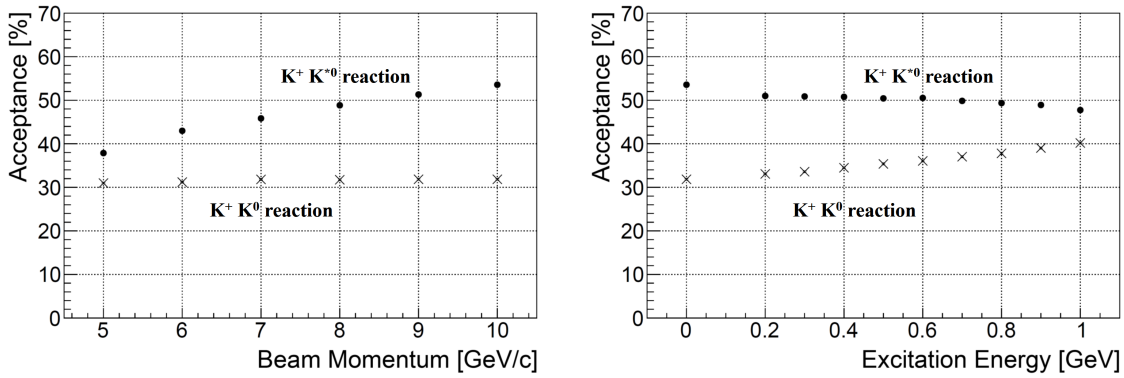

Figure 11: Detector acceptance for the Ω^--produced events (ground state) as a function of the incident kaon momentum (left), and that for the Ω^*-produced events as a function of the excitation energy at the incident momentum of 10 GeV/c (right). The filled circles and X markers represent the acceptances in the $K^-\ p \to \Omega^{(*)-}\ K^+\ K^{*0}$ and $K^-\ p \to \Omega^{(*)-}\ K^+\ K^0$ reactions, respectively. Here, detection of daughter particles are not required from the $\Omega^{(*)}$ decays.

4.2 Performance of the spectrometer for observing Ω^*s

The performance of the E50 spectrometer for the $\Omega^{(*)}$-produced events has been estimated by a Monte Carlo simulation based on Geant4. In this subsection, the acceptance of the $\Omega^{(*)}$-produced events, the experimental $\Omega^{(*)}$-mass resolution, and yield of the $\Omega^{(*)}$-produced events are described.

4.2.1 Acceptance of the $\Omega^{(*)}$-produced events

The $\Omega^{(*)}$-produced events are selected by using the $p(K^-, K^+K^{(*)0})$ missing mass (so called the missing-mass spectroscopy). It is necessary to detect the final-state $K^+\ K^+\ \pi^-$ ($K^+\ \pi^+\ \pi^-$) particles from $K^+\ K^{(*)0}$ emitted at forward angles. The acceptance for the $\Omega^{(*)}$-produced events is estimated so that all the $K^+\ K^+\ \pi^-$ ($K^+\ \pi^+\ \pi^-$) particles should be detected. Fig. 11(left) shows the detector acceptance for the Ω^--produced events (ground state) as a function of the incident kaon momentum. The detector acceptance for the Ω^--produced events are found to be 30%–50% and $\sim 30\%$ in the $K^-\ p \to \Omega^-\ K^+\ K^{*0}$ and $K^-\ p \to \Omega^-\ K^+\ K^0$ reactions, respectively. Here, the angular distribution of Ω^- production is assumed to be isotropic in the $K^-\ p$ center-of-mass (CM) frame. It should be noted that the acceptance includes the effects of final-state K^+ and $\pi^\pm$ decays. It gradually increases with increase of the incident kaon momentum in the $K^-\ p \to \Omega^-\ K^+\ K^{*0}$ reaction, and almost independent of the incident momentum below 10 GeV/c in $K^-\ p \to \Omega^-\ K^+\ K^0$. Figure 11(right) shows the acceptance for the Ω^*-produced events below the excitation energy of 1 GeV at the incident kaon momentum of 10 GeV/c. The angular distribution of Ω^* produc-

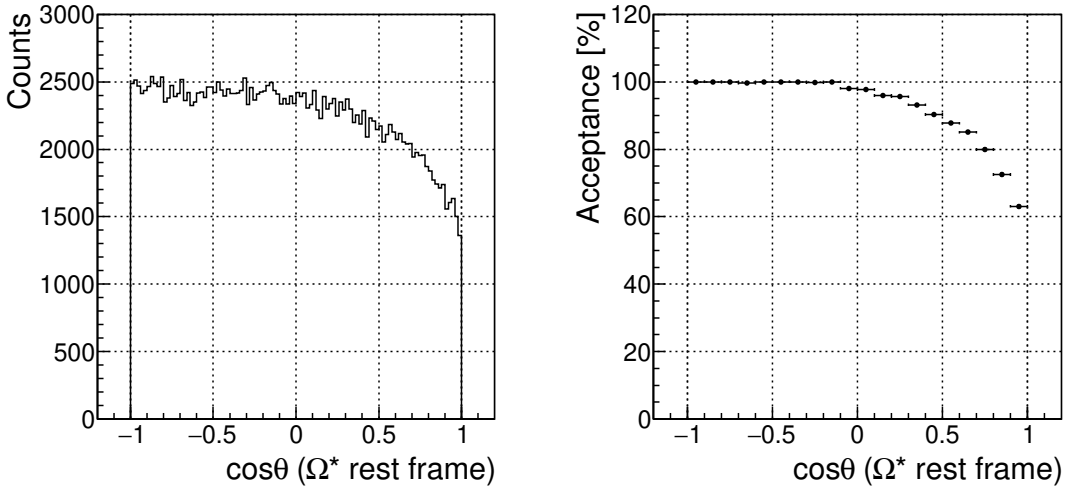

Figure 12: Angular distribution of Ξ^0 emission (left) and acceptance as a function of the Ξ^0 emission angle (right) in the rest frame of the produced Ω^{*-} (z-axis: opposite to the direction of the $K^+K^{(*)0}$ composite system produced together with Ω^*). The two-body $\Omega^- \to \Xi^0 K^-$ decay can be identified by additionally detecting the daughter K^-.

tion is also assumed to be isotropic in the K^- p CM frame. The acceptance becomes higher with increase of the excitation energy both in the K^- $p \to \Omega^{*-}$ K^+ K^{*0} and K^- $p \to \Omega^{*-}$ K^+ K^0 reactions. This is because K^+ K^{*0} (K^+ K^0) are likely to be emitted at forward angles where the E50 spectrometer has high acceptance in case of producing high-mass Ω^*s.

The daughter particles from the Ω^* decays are covered by the internal detectors. The horizontally-emitted particles finally comes to the detectors in front of the yoke, and the vertically-emitted to those on the pole pieces. Owing to these internal detectors, a wide coverage $\cos\theta_{\Xi^0} > -0.9$ is obtained for the polar angles of Ξ^0 emission (opposite to the direction of K^- emission) in the Ω^* rest frame from the two-body decay of Ω^* ($\Omega^{*-} \to \Xi^0$ K^-). The acceptance of the events detecting K^- (π^+ π^-) is found to be $\sim$95% ($\sim$90%) in the two-body $\Omega^{*-} \to \Xi^0$ K^- (three-body $\Omega^{*-} \to \Omega^-$ π^+ π^-) decay. It should be noted that the acceptance described above dose not include the effects of final-state K^- and $\pi^\pm$ decays. The effects of the in-flight decay of K^-s makes the acceptance lower by 10%. Figure 12 shows the acceptance of detecting the two-body $\Omega^{*-} \to \Xi^0$ K^- decay as a function of the Ξ^0 emission angle in the Ω^{*-} rest frame. Here, z-axis is defined to be opposite to the direction of the $K^+K^{(*)0}$ composite system produced together with Ω^*. The daughter K^- from the Ω^{*-} decay is emitted at forward angles in the laboratory frame, and the acceptance is high for detecting the $\Omega^{*-} \to \Xi^0$ K^- decay. Some acceptance drop is observed at the Ξ^0 emission angle of

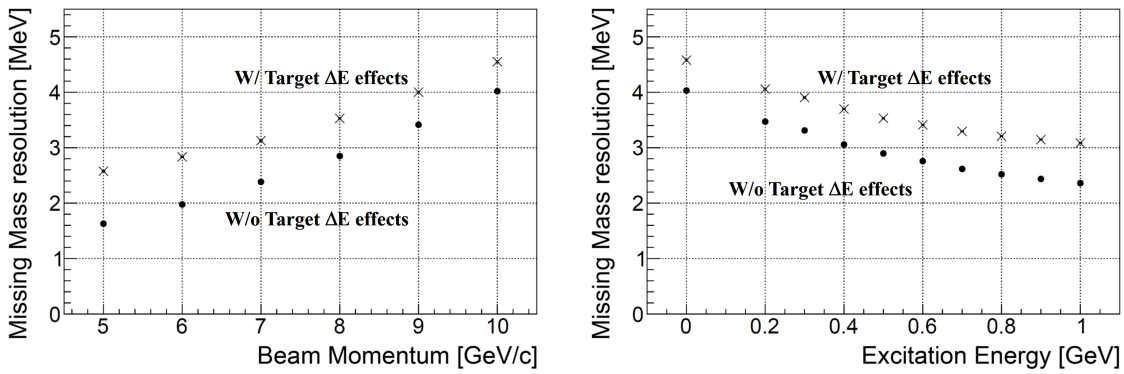

Figure 13: Resolution (σ) of the Ω^- mass as a function of the incident kaon momentum. The Ω^- mass is determined as the $p(K^-, K^+K^{*0})$ missing mass in the $K^-\ p \to \Omega^-\ K^+\ K^{*0}$ reaction (left), and from $p(K^-, K^+K^0)$ in $K^-\ p \to \Omega^-\ K^+\ K^0$ (right). The filled circles and X markers show the resolutions without and with the straggling effect of the energy loss in the target material, respectively.

$\cos\theta_{\Xi^0} \sim 1.0$. In this case, the corresponding K^-s are emitted at backward angles, and some of them are out of the angular coverage of the E50 spectrometer. Owing to high acceptance of the events with identifying the Ω^* decay, both the decay angular distribution and branching ratio can be determined.

4.2.2 $\Omega^{(*)}$-mass resolution

The resolution is estimated for the $\Omega^{(*)}$ mass, which is calculated as the $p(K^-, K^+K^{*0})$ missing mass in the $K^-\ p \to \Omega^{(*)-}\ K^+\ K^{*0}$ reaction, or the $p(K^-, K^+K^0)$ missing mass in the $K^-\ p \to \Omega^{(*)-}\ K^+\ K^0$ reaction. Here, the momentum resolutions are assumed as same as those in the planned E50 experiment for the incident kaon momentum, and each of the final-state $K^+\ K^+\ \pi^-$ and $K^+\ \pi^+\ \pi^-$ particles detected with the E50 spectrometer in the $K^-\ p \to \Omega^{(*)-}\ K^+\ K^{*0}$, and $K^-\ p \to \Omega^{(*)-}\ K^+\ K^0$, respectively. The incident momentum resolution assumed is a fixed value of $\Delta p_{\rm beam}/p_{\rm beam} = 0.1\%$ (σ). The momentum resolution assumed is $\Delta p_{\rm spec}/p_{\rm spec} = 0.2\%$ (σ) for 5-GeV/c particles detected with the E50 spectrometer, and is given by $\Delta p_{\rm spec}/p_{\rm spec} = 0.2\% \times p_{\rm spec}/\,(5\ {\rm GeV}/c)$ at a certain momentum $p_{\rm spec}$ for the detected particles. The 2-MeV (σ) straggling is incorporated for the energy loss in the target material, which corresponds to the 4-g/cm^3 thickness of the hydrogen target. The target thickness should be decided in the actual experiment considering the balance between the mass resolution and yield for Ω^*s.

Figure 13 shows the resolution (σ) of the $\Omega^{(*)-}$ mass as a function of the incident kaon momentum. The momentum becomes higher for each of the final-state $K^+\ K^+\ \pi^-$ ($K^+\ \pi^+\ \pi^-$) with increase of the incident momentum, deteriorating the resolution of the $\Omega^{(*)-}$ mass as well as that of the momentum of each final-state parti-

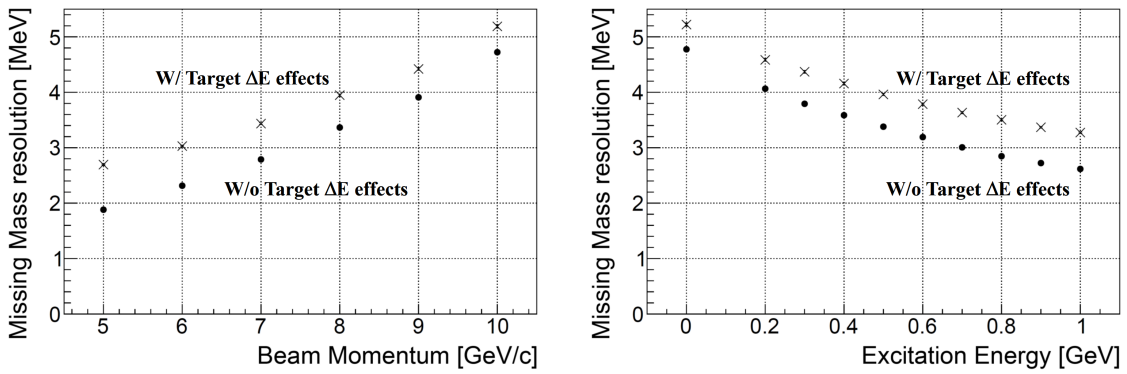

Figure 14: Resolution (σ) of the Ω^* mass as a function of the excitation energy at the incident kaon momentum of 10 GeV/c. The Ω^* mass is determined as the $p(K^-, K^+K^{*0})$ missing mass in the $K^-\ p \to \Omega^{*-}\ K^+\ K^{*0}$ reaction (left), and from $p(K^-, K^+K^0)$ in $K^-\ p \to \Omega^{*-}\ K^+\ K^0$ (right). The filled circles and X markers show the resolutions without and with the straggling effect of the energy loss in the target material, respectively.

cle. Figure 14 shows the resolution (σ) of the Ω^{*-} mass as a function of the excitation energy at the incident kaon momentum of 10 GeV/c. The mas resolution becomes higher with increase of the excitation energy since production of high-mass Ω^* makes the momentum lower for each final-state particle out of $K^+\ K^+\ \pi^-$ ($K^+\ \pi^+\ \pi^-$). The mass resolution is found to be 2.5–4.5 MeV (σ) depending on the incident kaon momentum and excitation energy. The high mass-resolution and narrow width of Ω^* (Γ is expected from several MeV to several tens of MeV for Ω^*s) enable us to observe Ω^{*-}s separably. Additionally, the Ω^{*-} width is expected to be measured directly since the mass resolution is comparable or better than it.

4.2.3 Yield of the Ω^*-produced events

We estimate the expected yields of the Ω^*-produced events detected with the E50 spectrometer at the K10 beam line. The existing data show the total cross sections range from 2.0 to 3.5 μb in the incident kaon momentum range 7–10 GeV/c for inclusive Ω^- production in the K^-p reaction: 0.5 ± 0.1 μb at 4.2 GeV/c [36, 37], 1.4 ± 0.6 μb at 6.5 GeV/c [38], 2.1 ± 0.3 μb at 8.25 GeV/c [39], 3.7 ± 0.9 μb at 10 GeV/c [40], and 3.9 ± 0.6 μb at 11 GeV/c [41]. The $K^-\ p \to \Omega^-\ K^+\ K^0$ reaction dominates in inclusive Ω^- production at incident kaon momentum below 10 GeV/c. Thus, we simply assume the cross sections are 2.0 and 3.5 μb for the $K^-\ p \to \Omega^-\ K^+\ K^0$ reaction at incident kaon momenta of 7 and 10 GeV/c, respectively. Since the total cross section increases rather linearly with increase of the incident kaon momentum, the total cross section is given by interpolating the 7- and 10-GeV/c cross sections to give a cross section at a certain incident momentum. Among the inclusive Ω^--produced events at 4.2 GeV/c

Table 3: Factors assumed for the yield estimation of Ω^* production, and expected yield of the Ω^*-produced events at the incident beam momentum of 8 GeV/c.

Reaction	$K^- p \to \Omega^{*-} K^+ K^{*0}$	$K^- p \to \Omega^{*-} K^+ K^0$
Cross section	2.50 μb	0.06 μb
Branching ratio	0.67 ($K^{*0} \to K^+\pi^-$)	0.35 ($K^0 \to \pi^+\pi^-$)
Beam intensity	7.0×10^6/spill (2-s duration in a 5.2-s cycle)	
Target thickness	4.0 g/cm^2 (57-cm-thick hydrogen)	
Acceptance (Ω^* production)	0.48	0.23
Tracking efficiency	0.90 (each particle)	
Particle identification	0.97 (each particle)	
Data acquisition efficiency	0.99 (Streaming DAQ)	
Total efficiency	0.66 (three-track events)	
Ω^* yield in a day	3.3×10^3	4.6×10^4
Ω^* yield in a 100-day beam time	3.3×10^5	4.6×10^6

in Ref. [37], the numbers of events containing K^0 and $K^+ \pi^-$ in the final state are 39 and 1, respectively. We assume that the total cross section of the $K^- p \to \Omega^- K^+ K^{*0}$ reaction is 1/40 that of $K^- p \to \Omega^- K^+ K^0$ at a fixed incident kaon momentum between 7 and 10 GeV/c. This assumption might not be realistic since a fraction of the $K^0 \to \pi\pi$ decay is 50% and since the $K^- p \to \Omega^- K^+ K^{*0}$ reaction is suppressed owing to the limited phase space at 4.2 GeV/c. We suppose these two effects are canceled out at incident kaon momenta of 7–10 GeV/c. Additionally, the production cross section of an Ω^{*-} is assumed to be the same as that of Ω^- depending on the reaction and incident kaon momentum.

The expected yield of Ω^*-produced events is estimated in the following assumptions: the cross section of Ω^* production is 0.06 μb and 2.50 μb at the incident kaon momentum of 8 GeV/c in the $K^- p \to \Omega^{*-} K^+ K^{*0}$ and $K^- p \to \Omega^{*-} K^+ K^0$ reactions, respectively, the tracking efficiency is 0.90 for each particle; the particle-identification efficiency is 0.97 for each particle; DAQ efficiency is 0.99; and the total efficiency is ~ 0.66 for three-track events. Acceptance of each reaction includes in-flight decay of scattered particles (both K^+ and $\pi^\pm$). Table 3 summarizes the factors assumed for the yield estimation of Ω^* production. The expected yields of Ω^*-produced events are 3.3×10^3 and 4.6×10^4 a day in the $K^- p \to \Omega^{*-} K^+ K^{*0}$ and $K^- p \to \Omega^{*-} K^+ K^0$ reactions, respectively. To obtain several 10^5 of the Ω^*-produced events, we need a 100-day beam time. In analysis of the decay angular distribution of Ω^*, the Ω^*-produced events may be combined for the $K^- p \to \Omega^{*-} K^+ K^{*0}$ and $K^- p \to \Omega^{*-} K^+ K^0$ reactions, and more than 10^5 Ω^*-produced events are available in a 100-day beam time. Suppose the branching ratio is 0.3 for the two-body $\Omega^{*-} \to \Xi^0 K^-$ decay, the expected yield is several 1000 for each bin of Ξ^0 emission angles divided into 20. Additional factors are

Table 4: Additional factors assumed for the yield estimation of the Ω^* decay angular distribution, and expected yield in each bin of the Ξ^0 emission angle in the rest frame of Ω^* divided into 20. The factors listed in this table are additional ones to those in Table 3.

Acceptance ($\Omega^{*-} \to \Xi^0\ K^-$ decay) (including in-flight decay of K^-)	0.86
Decay branching ratio ($\Omega^{*-} \to \Xi^0\ K^-$ decay)	0.30
Total efficiency for detecting K^-	0.75
$\Omega^{*-} \to \Xi^0\ K^-$ yield in a 100-day beam time	~ 4000 (each bin out of 20 angle bins)

listed in Table 4 to get the expected yields in the decay angular distribution.

4.3 Expected $\Omega^{(*)}$ mass spectrum

We have estimated how $\Omega^{(*)}$s are observed in the $p(K^-, K^+K^{*0})$ missing-mass spectrum. In this subsection, we show the expected $\Omega^{(*)}$-mass spectrum without any background processes, and with the background contributions estimated by a hadron-reaction generating code.

4.3.1 Spectrum for signal contributions

At first, we show the expected $\Omega^{(*)}$-mass spectrum without any background processes. The $\Omega^{(*)}$s considered are summarized in Table 5, which are taken from the Review of Particle Physics [1]. Additionally, we incorporate a Rope-like resonance $\Omega(2160)^-$ with the parameters described in Table 5. Figure 15 shows the expected $\Omega^{(*)}$-mass spectrum

Table 5: Mass and width parameters of $\Omega^{(*)}$s for estimating the expected $\Omega^{(*)}$-mass spectrum. We assume the parameters for $\Omega(2160)$ as expected, and take those for the others as listed in Review of Particle Physics [1].

$\Omega^{(*)}$	Mass [MeV]	Width [MeV]
$\Omega(2470)^-$	2470	72
$\Omega(2380)^-$	2380	26
$\Omega(2250)^-$	2250	55
$\Omega(2160)^-$	2160	100
$\Omega(2012)^-$	2012	6.4
Ω^-	1672	—

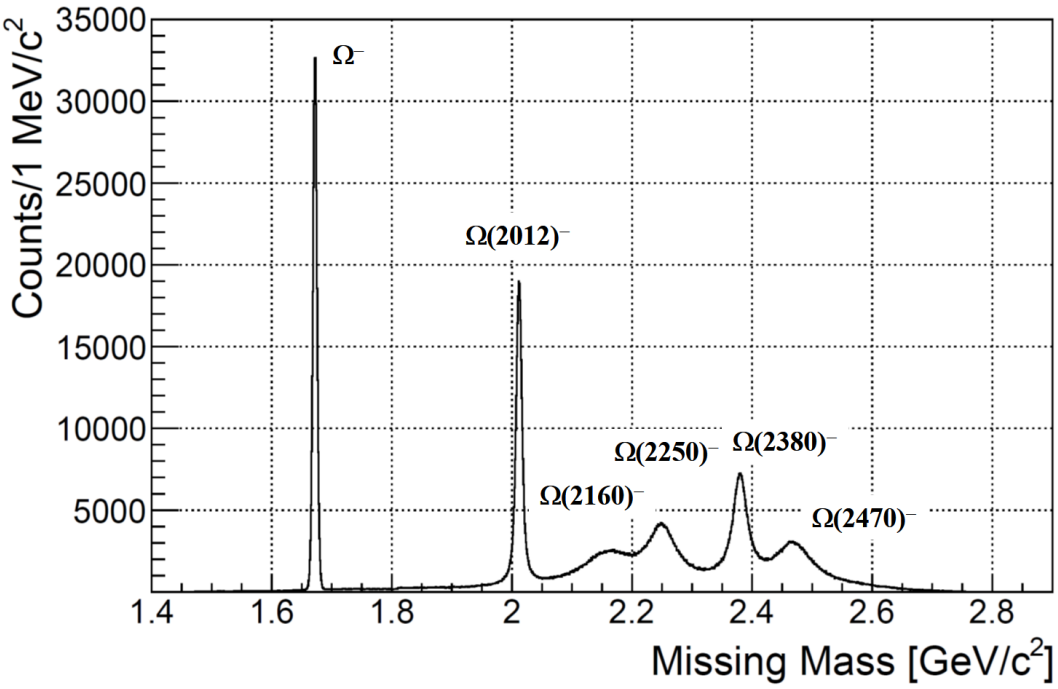

Figure 15: Expected $\Omega^{(*)}$-mass spectrum without any background processes at the incident kaon momentum of 8 GeV/c in a 100-day beam time. The spectrum is obtained by the $p(K^-, K^+K^{*0})$ missing mass for the generated $\Omega^{(*)}$-produced events.

without any background processes at the incident kaon momentum of 8 GeV/c. Here, the $\Omega^{(*)}$ mass is given by the $p(K^-, K^+K^{*0})$ missing mass, and the number of produced $\Omega^{(*)}$s is fixed at 3.3×10^5 for each $\Omega^{(*)}$ corresponding to a 100-day beam time. Peaks are separably observed for narrow $\Omega^{(*)}$s with a width narrower than 30 MeV, and those are clearly distinguished from others even for rather wide ones. It should be noted that all the experimental resolutions are included: momentum resolution, angular resolution, and straggling of the energy loss in the target material.

Since the number of events is $\sim 1.0 \times 10^5$ in each peak, the precision of the mass determination in this spectrum is better than 1 MeV depending on the width of the corresponding $\Omega^{(*)}$. To get accuracy of the mass determination, the absolute momentum scale in the spectrometer is required to be calibrated carefully. We can use various peaks corresponding to hyperons and other baryons in similar mass spectra. Thus, the accuracy expected is also better than 1 MeV after the calibration.

It is difficult to accurately determine the width of an $\Omega^{(*)}$. The observed peak must be modified by the experimental mass resolution of 2.5–4.5 MeV (σ). The peak may be different in shape from the Breit-Wigner function owing to the overlap with other peaks and background contributions, and interference with other processes. The

Table 6: K^- p cross sections for the background contributions estimated by JAM together with those assumed for the signal Ω^*-produced processes. The ratios of the cross sections of the Ω^*-produced K^- $p \to \Omega^{*-}$ K^+ K^0 and K^- $p \to \Omega^{*-}$ K^+ K^{*0} reactions to the background K^- $p \to K^+$ π^- X and $K^- p \to K^+$ K^+ π^- X are also listed, respectively.

Beam [GeV/c]	$\sigma_{\rm tot}$ [mb]	$\sigma_{K^+\,\pi^-}$ [μb]	$\sigma_{K^+\,K^+\,\pi^-}$ [μb]	$\sigma_{\Omega^*\,K^+\,K^0}$ [μb]	$\sigma_{\Omega^*\,K^+\,K^{*0}}$ [μb]	Ratio [%] $\frac{\sigma_{\Omega^*\,K^+\,K^0}}{\sigma_{K^+\,\pi^-}}$	Ratio [%] $\frac{\sigma_{\Omega^*\,K^+\,K^{*0}}}{\sigma_{K^+\,K^+\,\pi^-}}$
7.0	25.6	463	1.80	2.00	0.050	0.43	2.8
8.0	23.6	503	2.46	2.50	0.063	0.50	2.6
9.0	23.2	548	3.16	3.00	0.075	0.55	2.4
10.0	22.6	585	4.22	3.50	0.088	0.60	2.0

accuracy of the width determination expected is better than 1 MeV for an isolated Breit-Wigner peak with a width of 10 MeV. We expect the accuracy of the width determination is better than a few MeV for high-mass Ω^*s, which are overlapped with other contributions.

4.3.2 Spectrum for background contributions

It is difficult to estimate the background contribution correctly in the $\Omega^{(*)}$-mass spectrum obtained from the K^- p reaction for several-GeV/c incident kaons. Available experimental data are quite limited in this momentum range, and we cannot estimate inclusive cross sections or multiplicities of generated particles even if we find some exclusive cross sections in a particular reaction. Thus, we use a hadron-reaction generating code called JAM (version 1.90597) [42] for the background estimation as usual. JAM includes many elementary reaction processes at wide CM energies, covering the resonance region ($\sqrt{s} < 4$ GeV), the string region ($4 < \sqrt{s} < 10$ GeV), and the perturbative-QCD (pQCD) region ($\sqrt{s} > 10$ GeV).

The string region is of interest in the proposed experiment. In this region, the string-string scattering processes mainly generate hadrons. The hadronization process is described in the Lund string model [43], which is also adopted in another hadron-reaction generating code called PYTHIA [44]. Adjusted in JAM to reproduce the existing experimental data are the conditions of the string-string scattering and hadronization processes: no string-string scattering before hadronization, no color-flow during the string generation, and the production ratios of the generated hadron resonances. Those conditions and hadron resonances considered are different from those in PYTHIA. Here, we do not use PYTHIA but JAM since we have found JAM reproduces

the experimental data better than PYTHIA at incident momenta of several GeV/c[§].

Table 6 shows the K^- p cross sections for the background contributions estimated by JAM together with those assumed for the signal Ω^*-produced processes. We investigate K^+ and K^+ K^+ π^- production as background contributions. The cross section for the K^+ K^+ π^--produced events is found to be two-order smaller than that for K^+-produced events. Thus, the $\Omega^{(*)}$-mass spectrum obtained in the K^- $p \to \Omega^{(*)-}$ K^+ K^{*0} reaction is expected to have low background as compared with that in the K^- $p \to \Omega^{(*)-}$ K^+ K^0. Additionally, some of K_0 candidates reconstructed from $\pi^+\pi^-$ can be $\bar{K}$ so that the $\Omega^{(*)}$-mass spectrum includes contributions from Λ^* and Σ^*-produced events. It is necessary to detect not K^0 but K^{*0} for reducing background contributions in the $\Omega^{(*)}$-mass spectrum. We can obtain the $\Omega^{(*)}$-mass spectrum with high signal-to-noise (S/N) ratio from the $p(K^-, K^+K^{*0})$ missing mass which gives only an $S = -3$ system.

4.3.3 Spectrum for the sum of signal and background contributions

Figure 16 shows the expected $\Omega^{(*)}$-mass spectrum including background contributions at the incident kaon momentum of 8 GeV/c. The $\Omega^{(*)}$ mass is calculated by the $p(K^-, K^+K^{*0})$ missing mass, and the cross section of K^- $p \to \Omega^{(*)-}$ K^+ K^{0*} for each $\Omega^{(*)}$ is assumed to be 63 nb. The number of events for each peak is $\sim 3.3 \times 10^5$, which can be obtained in a 100-day beam time. Since the Roper-like Ω^*, $\Omega(2160)^-$, has a broad width of 100 MeV, the events corresponding to it is distributed in a wide range, generating not a peak or bump but a shoulder. A peak or bump is clearly observed corresponding to each of the other Ω^*s with the narrower widths. It is concluded that we can measure the $\Omega^{(*)}$-mass spectrum with high S/N ratio at the K10 beam line. Even if the cross section smaller by a factor of 1/3, we can still recognize the Ω^-, $\Omega(2012)^-$, $\Omega(2250)^-$, and $\Omega(2380)^-$ peaks. Figures 17 and 18 show the expected $\Omega^{(*)}$-mass spectra including background contributions at the incident kaon momentum of 8 GeV/c by reducing Ω^* production cross sections by a factor of 1/1, 1/3, 1/10 and 1/30. If the Ω^*-production cross section is smaller by 1/10 than that in the original assumption (63 nb), it is difficult to identify Ω^* peaks except for the ground-state Ω^- and first-excited $\Omega(2012)^-$. In this case, an additional method is necessary to reduce the background contributions for finding an Ω^* with a broad width.

4.3.4 Possible background reduction

We plan to determine the mass spectrum of Ω^*s originally without using information on the daughter particles from their decay. Here, we consider to use the daughter particles for improving the S/N ratio in the mass spectrum. Since the $\Omega^{*-} \to \Xi^0$ K^- decay channel is expected to have a large branching ratio, we focus on extracting the events corresponding to this channel from now on. It should be noted that generated Ω^{*-}

[§]We have investigated both the codes, and compared with the experimental data for the background studies in the E50 experiment for charmed baryon spectroscopy [28].

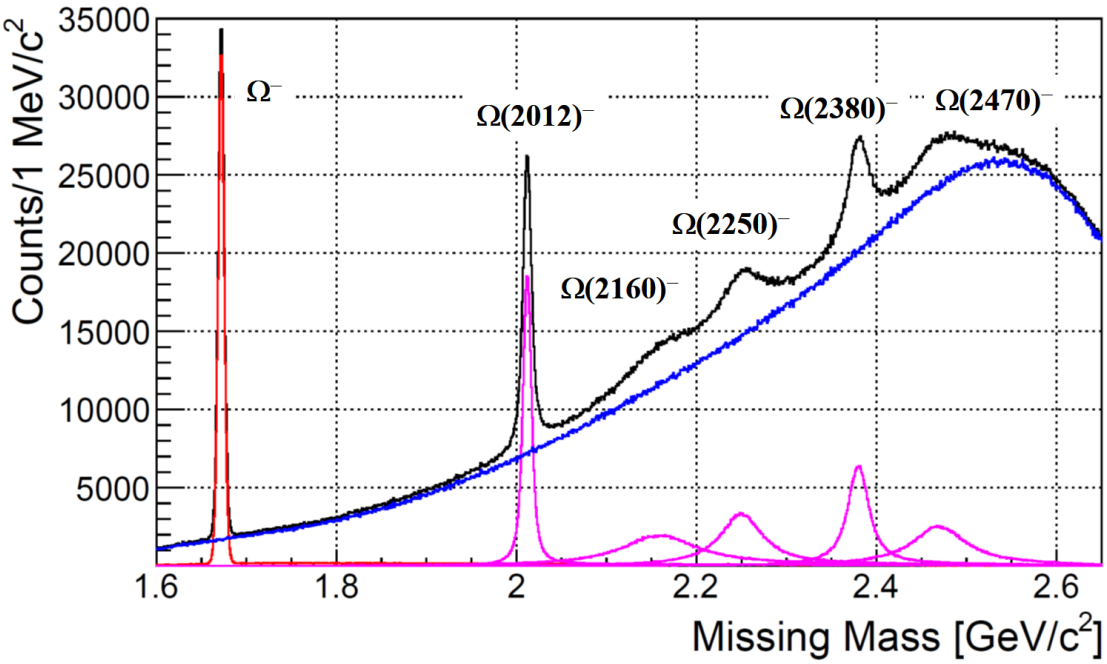

Figure 16: Expected $\Omega^{(*)-}$-mass spectrum including background contributions at the incident kaon momentum of 8 GeV/c in a 100-day beam time. The spectrum is obtained by the $p(K^-, K^+\ K^{*0})$ missing mass for the generated $\Omega^{(*)-}$-produced events and background processes. The smooth blue curve represent the background contribution estimated by JAM, and the contributions from the ground-state Ω^- and Ω^{*-}s are also plotted in red and in magenta, respectively. The missing system in $p(K^-, K^+K^{*0})$ gives $S = -3$ eliminating huge background from Σ^*-produced events.

can decay in several channels according to the JAM parameters. Figure 19(a) shows the $p(K^-, K^+K^{*0}K^-)$ missing-mass spectrum for the background events generated by JAM. In Fig. 19(a), peaks corresponding to Λ, Ξ^0, and Ξ^{*0} are observed. The generated events in JAM include those from $K^-\ p \to K^+\ K^{*0}\ K^-\ \Xi^{0(*)}$, showing the Ξ^0 and Ξ^{*0} peaks. The events forming the Λ peak come mainly from the decay of the ground-state Ω^- which is included in JAM. It also comes from the $K^-\ p \to \Xi^- K^+ \phi$ reaction followed by the $\Xi^- \to \Lambda\pi^-$ and $\phi \to K^+\ K^-$ decays. Since the width of K^{*0} is rather broad, K^+ and π^- in the final-state of this reaction sequence can be identified as K^{*0}. Detailed analysis of the production and decay vertices is expected to remove this background process. Figure 19(b) shows the $p(K^-, K^+K^{*0})$ missing-mass spectrum for the background events. A peak corresponding to Ω^- can be observed clearly. Above this peak, a huge amount of the continuum background events are observed which prevent us from observing highly-excited Ω^*s. Figure 19(c) shows the

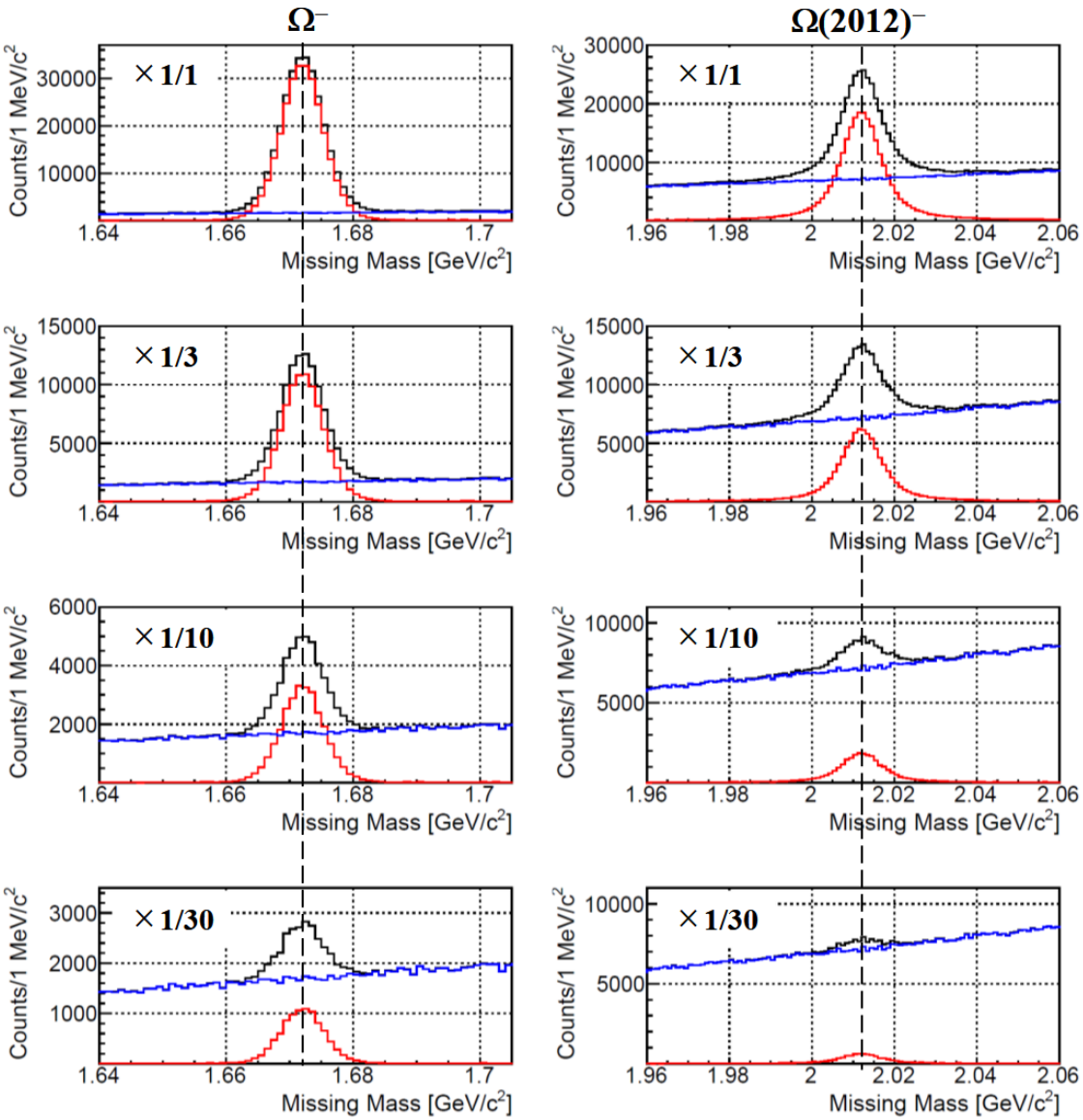

Figure 17: Expected $\Omega^{(*)}$-mass spectra, or the $p(K^-, K^+\ K^{*0})$ missing mass spectra, including background contributions at the incident kaon momentum of 8 GeV/c in a 100-day beam time by reducing Ω^* production cross sections by a factor of 1/1, 1/3, 1/10 and 1/30 from the top to bottom panels. The mass spectra are expanded for the ground-state Ω^- and $\Omega(2012)^-$ in the left and right panels, respectively.

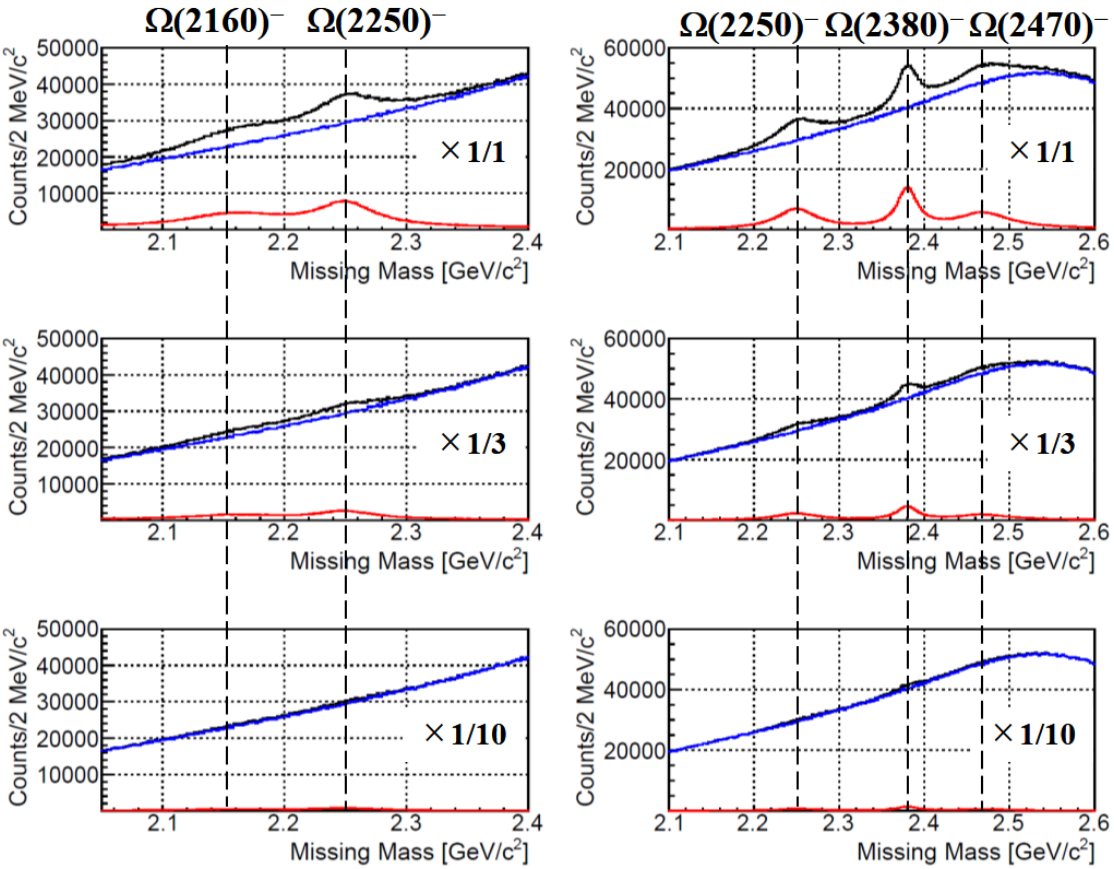

Figure 18: Expected Ω^*-mass spectra, or the $p(K^-, K^+\ K^{*0})$ missing mass spectra, including background contributions at the incident kaon momentum of 8 GeV/c in a 100-day beam time by reducing Ω^* production cross sections by a factor of 1/1, 1/3 and 1/10 from the top to bottom panels. The mass spectra are expanded for $\Omega(2160)^-$ and high-mass Ω^*s in the left and right panels, respectively.

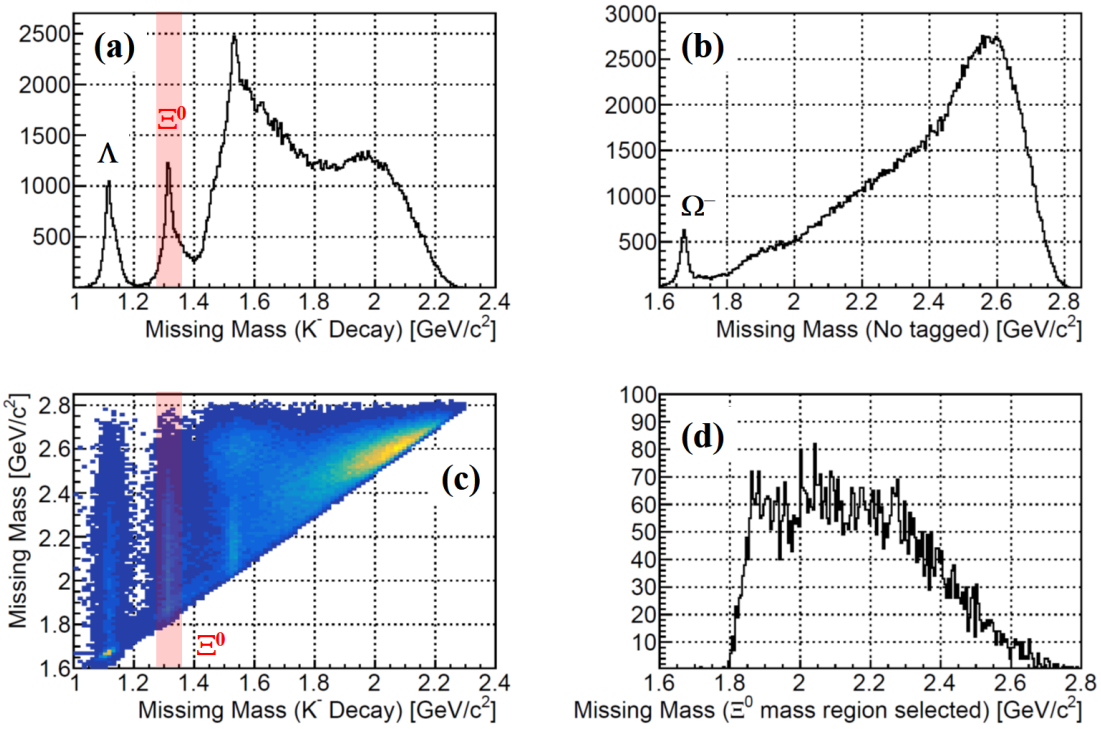

Figure 19: (a) $p(K^-, K^+K^{*0}K^-)$ missing-mass spectrum for the background events generated by JAM. (b) $p(K^-, K^+K^{*0})$ missing-mass spectrum for the background events. (c) Correlation between the the $p(K^-, K^+K^{*0})$ and the $p(K^-, K^+K^{*0}K^-)$ missing masses for the background events. (d) $p(K^-, K^+K^{*0})$ missing-mass spectrum for the background events after selecting the events near Ξ^0 mass in the $p(K^-, K^+K^{*0}K^-)$ missing-mass spectrum.

correlation plot between the the $p(K^-, K^+K^{*0})$ and the $p(K^-, K^+K^{*0}K^-)$ missing masses. By selecting the events near Ξ^0 mass in the $p(K^-, K^+K^{*0}K^-)$ missing mass spectrum, we can remove huge background concentrated as shown in Fig, 19(c) at a $p(K^-, K^+K^{*0})$ missing mass of $\sim$ 2.6 GeV and a $p(K^-, K^+K^{*0}K^-)$ missing mass of $\sim$ 2.1 GeV. Figure 19(d) shows the $p(K^-, K^+K^{*0})$ missing-mass spectrum for the background events after selecting the events near Ξ^0 mass in the $p(K^-, K^+K^{*0}K^-)$ missing mass spectrum. As compared with Fig. 19(b), the background level has been reduced by a factor of /10 or 1/100. The S/N ratio is much improved since the branching ratio assumed must be ~ 0.3 for the $\Omega^{*-} \to \Xi^0\ K^-$ decay.

Selecting the events containing Ξ^0 as a daughter particle from the Ω^* decay is effective at background reduction in the Ω^*-mass spectrum if the branching ratio is ~ 0.3 for the $\Omega^{*-} \to \Xi^0\ K^-$ decay. As shown in Figs. 20 and 21, the S/N ratio is improved by a factor of 1/10 for the high-mass Ω^*s so that we can recognize Ω^*s with

a broad width even when the cross section is smaller than that originally assumed. We can also find the $\Omega(2160)^-$ or the Roper-like state having a broad width of 100 MeV even if the cross section is smaller by 1/10 than that in the original assumption. Since Ξ^0 is a rather stable particle, we can recognize its flight path before decaying. Thus, detailed analysis of the production and decay vertices of an Ω^* would help us to get the further higher S/N ratio.

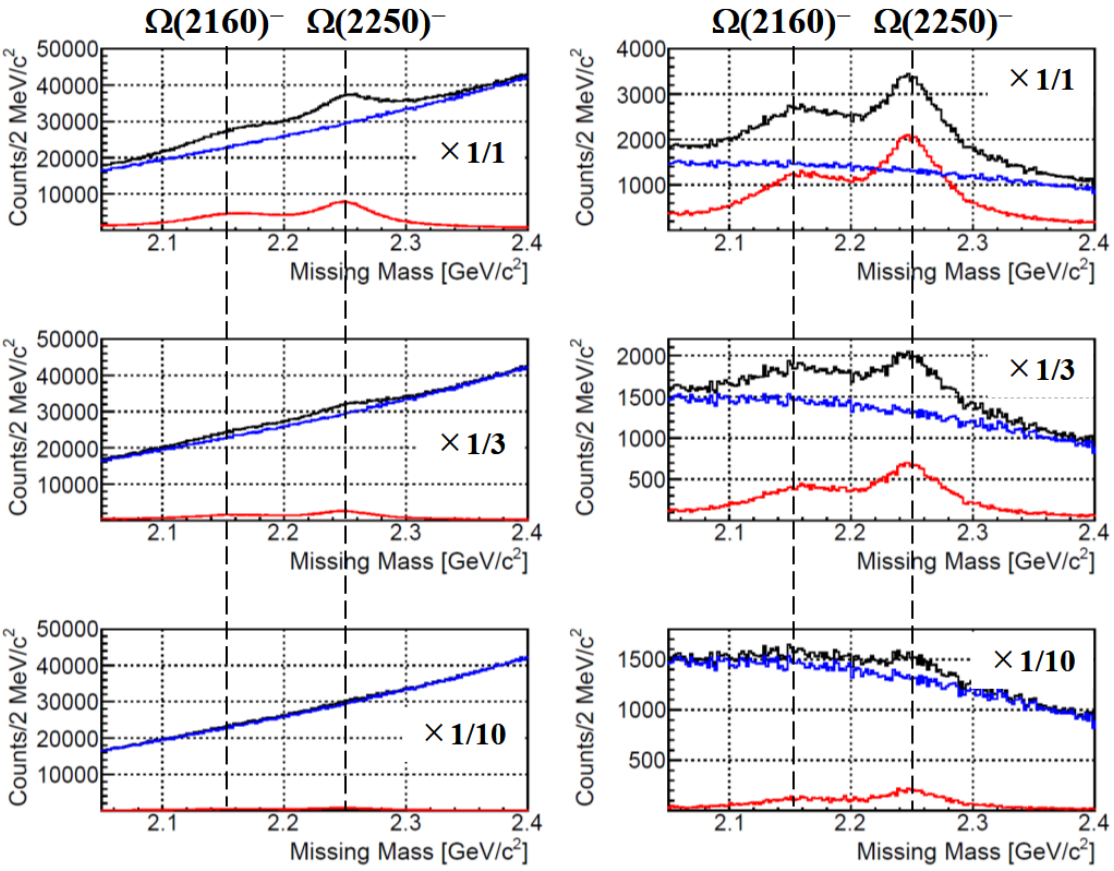

Figure 20: Expected Ω^*-mass spectra, or the $p(K^-, K^+\ K^{*0})$ missing mass spectra, including background contributions at the incident kaon momentum of 8 GeV/c in a 100-day beam time by reducing Ω^* production cross sections by a factor of 1/1, 1/3 and 1/10 from the top to bottom panels. The left panel corresponds to the spectra that any requirement is applied for the $p(K^-, K^+K^{*0}K^-)$ missing mass. The right panel corresponds to the spectra that the events are selected near the Ξ^0 mass in the $p(K^-, K^+K^{*0}K^-)$ missing-mass spectrum. The mass spectra are expanded for $\Omega(2160)^-$.

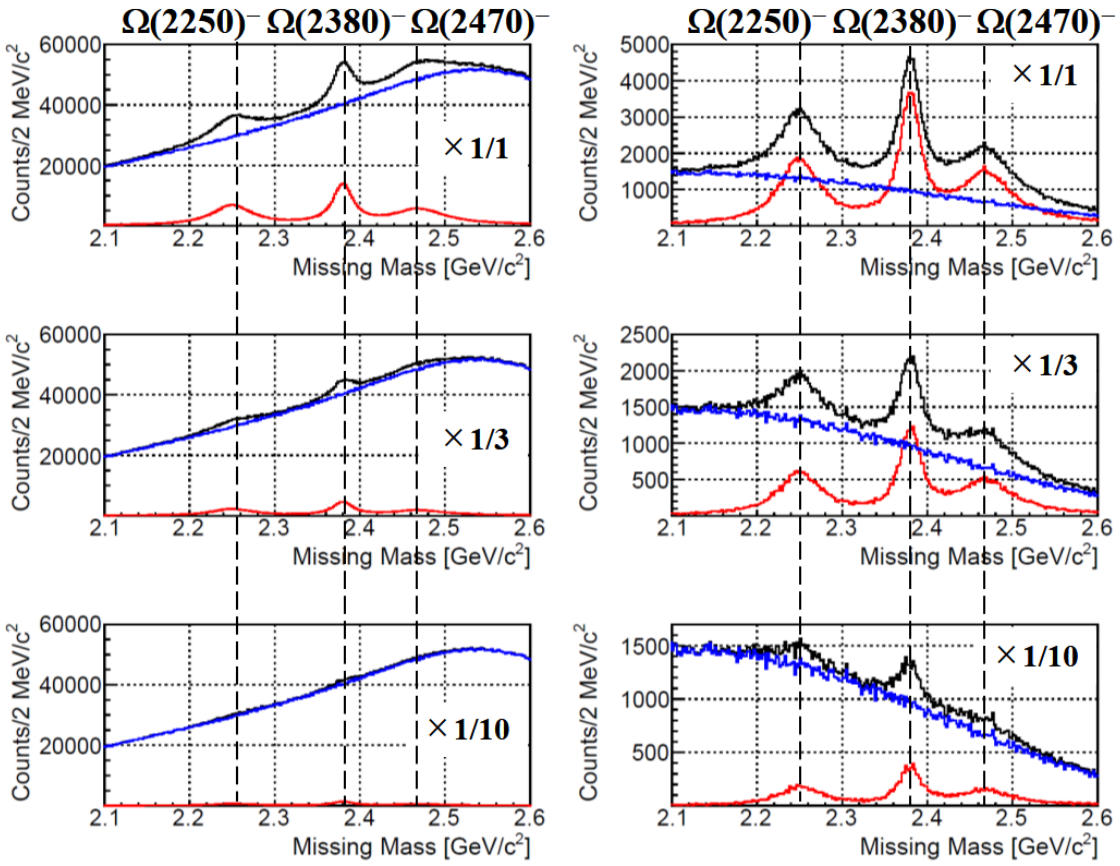

Figure 21: Expected Ω^*-mass spectrum, or the $p(K^-, K^+\ K^{*0})$ missing mass spectra, including background contributions at the incident kaon momentum of 8 GeV/c in a 100-day beam time by reducing Ω^*-production cross sections by a factor of 1/1, 1/3 and 1/10 from the top to bottom panels. The left panel corresponds to the spectra that any requirement is applied for the $p(K^-, K^+K^{*0}K^-)$ missing mass. The right panel corresponds to the spectra that the events are selected near the Ξ^0 mass in the $p(K^-, K^+K^{*0}K^-)$ missing-mass spectrum. The mass spectra are expanded for high-mass Ω^*s.

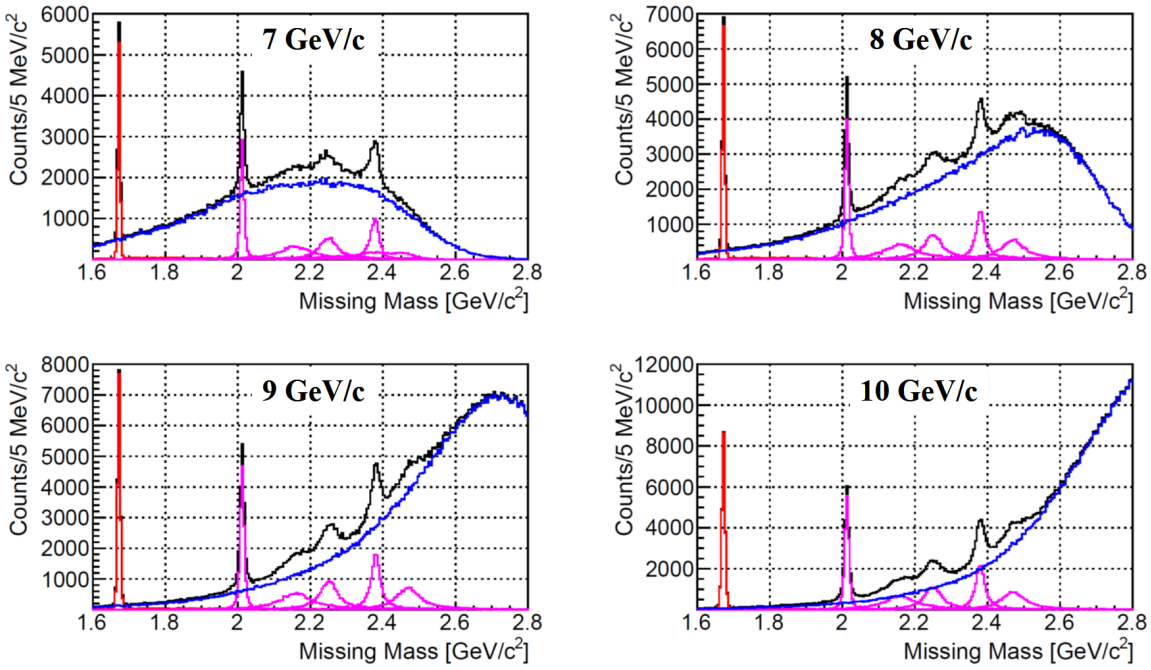

Figure 22: Expected $\Omega^{(*)}$-mass spectra, or the $p(K^-, K^+\ K^{*0})$ missing mass spectra, including background contributions at the incident kaon momenta of 7 GeV/c (top-left), 8 GeV/c (top-right), 9 GeV/c (bottom-left), and 10 GeV/c (bottom-right) in a 3-day beam time. The smooth blue curve represent the background contribution estimated by JAM, and the contributions from the ground-state Ω and Ω^*s are also plotted in red and in magenta.

4.3.5 Different incident kaon momenta

Thus far, shown are only the expected $\Omega^{(*)}$-mass spectra at the incident kaon momentum of 8 GeV/c. We also estimate those at several different incident kaon momenta. Figure 22 shows the expected $\Omega^{(*)}$-mass spectra expected a the incident kaon momenta of 7, 8, 9, and 10 GeV/c. The excitation-energy range covered in the measurement becomes wider with increase of the incident kaon momentum, and high-mass Ω^*s are likely to be observed up to the excitation energy of 1.5 GeV at the highest incident kaon momentum of 10 GeV/c. Within the excitation-energy coverage, all the peaks corresponding to Ω^*s are clearly observed with high S/N ratios. It is important to measure the Ω^*-mass spectra at different incident kaon momenta. A fake structure may appear caused by some kinematic effects since the measured spectrum reflects the appearance of a resonance in other system of the final-state particles than that corresponding to Ω^*s. This kind of kinematic effects are observed in a different shape at a different incident kaon momentum. The mass spectra with several incident momenta enable us to identify fake structures coming from the kinematic effects. The

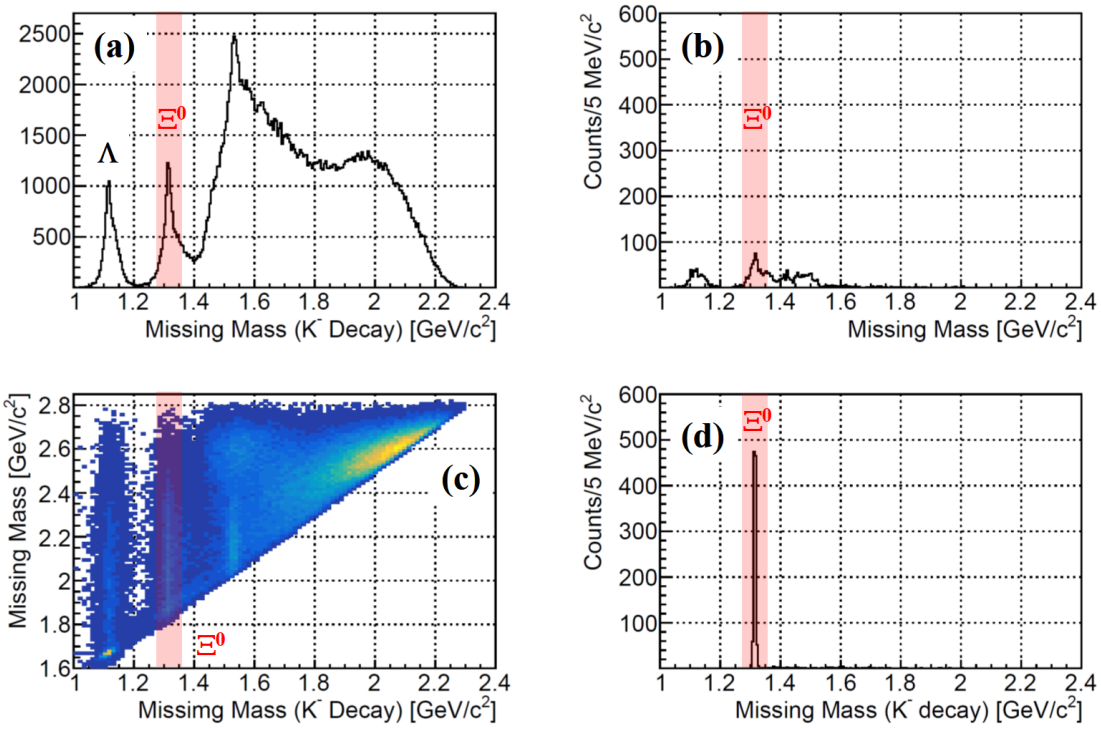

Figure 23: (a) $p(K^-, K^+\ K^{*0}\ K^-)$ missing-mass spectrum for the background events estimated by JAM (same as Fig. 19(a)). (b) $p(K^-, K^+\ K^{*0}\ K^-)$ missing-mass spectrum for the background events after selecting the events near $\Omega^-(2012)$ mass in the $p(K^-, K^+\ K^{*0})$ missing mass spectrum. (c) Correlation between the the $p(K^-, K^+\ K^{*0})$ and the $p(K^-, K^+\ K^{*0}\ K^-)$ missing masses for the background events. (d) $p(K^-, K^+\ K^{*0})$ missing-mass spectrum for the $\Omega(2012)^-$-produced events after selecting the events near the $\Omega(2012)^-$ mass in the $p(K^-, K^+\ K^{*0})$ missing mass spectrum.

mass spectra with different incident momenta are also useful for determination of the the Ω^{*-} widths. The optimum incident kaon momentum is different for different excitation energies since the sensitivity of the width determination highly depends on the background level and background shape.

4.4 Decay angular distribution

We show here how to determine the angular distribution of Ξ^0 emission (decay angular distribution) of an Ω^{*-} in the two-body $\Omega^{*-} \to \Xi^0\ K^-$ decay. The branching ratio assumed is 0.3 for this decay channel. In principle, the Ω^{*-}-produced events are identified by using the $p(K^-, K^+\ K^{*0})$ missing mass. The decay angular distribution can be given additionally detecting the daughter K^- from the Ω^{*-} decay. Here, we focus

on deducing the decay angular distribution for $\Omega(2012)^-$ as an Ω^{*-}. We select the events that the $p(K^-, K^+K^{*0})$ and $p(K^-, K^+K^{*0}K^-)$ missing masses are close to the $\Omega(2012)^-$ and Ξ^0 masses, respectively. The selected region is indicated in Fig. 23(c). Figure 23(b) shows the $p(K^-, K^+K^{*0}K^-)$ missing-mass spectrum for the background events after selecting the events near the $\Omega(2012)^-$ mass in the $p(K^-, K^+K^{*0})$ missing-mass spectrum, and Figure 23(d) for the $\Omega(2012)^-$-produced events. Let us look at the $p(K^-, K^+K^{*0}K^-)$ missing-mass spectra as shown in Fig. 23 (b) for the background contributions and in Fig. 23 (d) for $\Omega(2012)^-$ production. The background contributions are well suppressed and distributed in a wider range as compared with $\Omega(2012)^-$ production. Thus, a side-band subtraction method can be used to extract the $\Omega(2012)^-$-produced events for deduction of the decay angular distribution. The decay angular distribution can be obtained similarly to $\Omega(2012)^-$ for the other Ω^*s.

We estimate the decay angular distribution in the rest frame of the produced Ω^{*-}. Here, z-axis is defined to be opposite to the direction of the K^+K^{*0} composite system. Figure 24 shows the acceptance-corrected decay angular distribution. The isotropic decay angular distributions are obtained according to isotropic event generation of the $\Omega^{*-} \to \Xi^0\ K^-$ decay in the simulation. The decay angular distribution for the $\Omega^*(J^P) \to \Xi^0(1/2^+)\bar{K^-}(0^-)$ decay is expressed using the spin-density matrix (SDM) of $\Omega^*(J^P)$ as

$$\begin{array}{lll} W(\theta) \propto & 1 & \text{for } J = 1/2, \\ W(\theta) \propto & 3\rho_{33}\sin^2\theta + \rho_{11}(1 + 3\cos^2\theta) & \text{for } J = 3/2, \text{and} \\ W(\theta) \propto & 5\rho_{55}(1 - \cos^2\theta)^2 + \rho_{33}(1 + 14\cos^2\theta - 15\cos^4\theta) & \\ & +2\rho_{11}(1 - 2\cos^2\theta + 5\cos^4\theta) & \text{for } J = 5/2. \end{array} \tag{13}$$

The azimuthal-angle asymmetry is simply ignored here, which is expected to be observed as the angle between the production and decay planes. The diagonal of elements of SDM, ρ_{2J2J}, can be determined by fitting a function expressed by Eq. (13) to the observed angular distribution. In Fig. 24, the $W(\theta)$ functions corresponding to the isotropic generation and the case with $\rho_{11} = 0.5,\ \rho_{33} = 0,\ \rho_{55} = 0$ for $J = 5/2$ are also plotted. A flat decay angular distribution can be explained by any J with some J_z sub-population: always for $J = 1/2$, $\rho_{11} = \rho_{33} = 1/4$ for $J = 3/2$, and $\rho_{11} = \rho_{33} = \rho_{55} = 1/6$ for $J = 5/2$. When the angular distribution shows some structure, the ratio of ρ_{2J2J}s are expected to be determined with an error of $\sim$1% for a certain J. We can perform more detailed analysis for determining the spin for the Ω^* of interest by combining other information such as the branching ratio. When we observe a sequential process $K^-p \to \Xi^{*0}K^{*0}$ followed by $\Xi^{*0} \to \Omega^{*-}K^+$, we can determine the spin-parity of Ω^{*-} from the angular correlation between K^{*0} and K^+ at the Ω^* production stage.

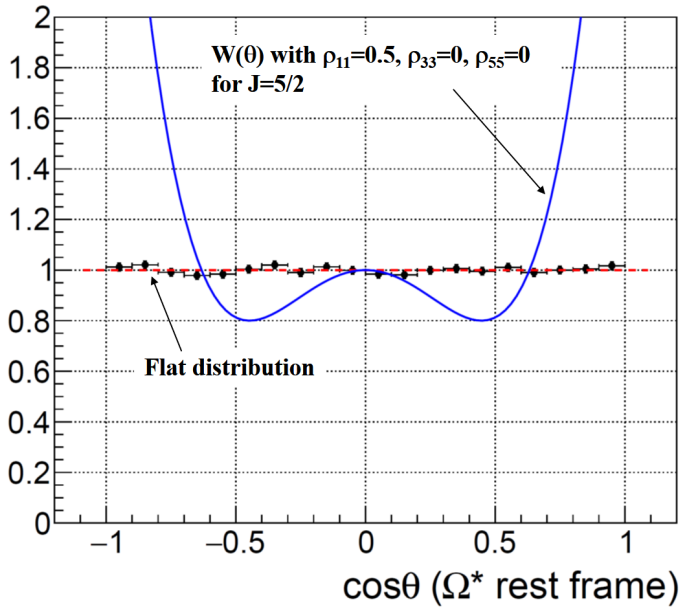

Figure 24: Acceptance-corrected decay angular distribution of Ξ^0 emission in the reset frame of Ω^* (z-axis: opposite to the direction of the K^+K^{*0} composite system). Isotropic distributions corresponding to the event generation are obtained correctly. The data are plotted only with statistical errors. The $W(\theta)$ functions corresponding to the isotropic generation and the case with $\rho_{11} = 0.5,\ \rho_{33} = 0,\ \rho_{55} = 0$ for $J = 5/2$ are also plotted in the red dashed and blue curves, respectively.

5 Summary

The aim of this project is to reveal unsolved issues in baryon spectroscopy. We focus our investigations on Ω baryons where experimental and theoretical studies have not been fully performed yet. We measure $1/2^-$ and $3/2^-$ states of Ω baryons by which we investigate the origin of the LS splitting. The study of the states are also related to answering the question of their structure, whether they are quark excited states or hadronic molecules. We also measure the mass and width of the Roper-like state of Ω of expected spin and parity $1/2^+$. We will confirm whether the mass appears at the position that is expected from the systematics in the corresponding states with various flavor contents. We extract the size of "quark core" region by measuring the decay width. We attempt to link the results of the above studies to the understanding of non-perturbative dynamics QCD.

By using the high-intensity K^- beam realized at the K10 beam line together with the large-acceptance spectrometer, more than 3×10^5 Ω^*-produced events are expected in a 100-day beam time for a Ω^* with a production cross section of 63 nb. The $S = -3$ tagging $p(K^-, K^+K^{*0})$ missing-mass spectrum gives the $\Omega^{(*)}$-mass spectrum with a high S/N ratio. The mass resolution is expeted to be better than 5 MeV (σ) which is enough to observe Ω^*s separably and directly measure their widths. By selecting the events with identifying the daughter Ξ^0 from the Ω^* decay, we can find Ω^*s with a width narrower than 100 MeV. The decay angular distribution enables us to determine the spin of an Ω^*. We can conclude that the proposed experiment is feasible at the K10 beam line for Ω baryon spectroscopy.

Acknowledgments

We would like to express our gratitude to Dr. H. Nemura, Prof. D. Jido, Mr. Iizawa, Prof. S. Kumano, Prof. A. Ohnishi, Prof. T. Hyodo, Dr. Y. Kamiya, Prof. M. Oka, Prof. T. Hatsuda, Prof. M. Karliner, Prof. C. Z. Yuan, and Prof. Q. F. Lyu for their valuable contributions to this project through intensive discussions.

A Baryon spectroscopy with heavy flavors

A.1 Baryon with a single heavy quark and two-light quarks

To study dynamics of light degrees of freedom such as the light constituent quarks and diquarks, it is helpful to introduce a heavy flavor in a baryon, where the heavy quark behaves as an inert particle. In excited states, a collective motion of two light quarks to a heavy quark (λ mode) is separated in kinematics from a relative motion between the two light quarks (ρ mode), as shown in Fig 25. The orbital excitation energy of the λ mode becomes lower than that of the ρ mode by a factor $[3m_Q/(2m_q + m_Q)]^{1/2}$ approximately, where m_Q and m_q are masses of the heavy and light quark, respectively. It is known as the so-called isotope shift.

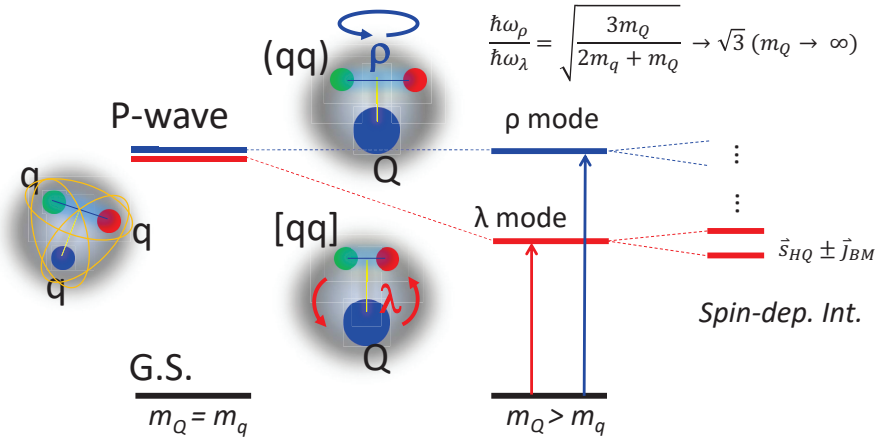

Figure 25: Schematic illustration of the orbital excitations for the λ and ρ modes in a baryon with a heavy quark. The λ and ρ modes are degenerated in a light baryon.

It is known that the QCD has the so-called heavy quark spin symmetry. Namely, the heavy quark spin is conserved in the heavy quark mass limit ($m_Q \to \infty$). Since the color-magnetic (color-spin) interaction between quarks is proportional to the inverse of the relevant quark masses, spin-dependent interactions to the heavier quark become weaker as the quark mass increases, being zero in the heavy quark mass limit. As a result, the heavy-quark spin (s_Q=1/2) as well as a baryon spin (J), and hence the rest spin (the so-called Brown-muck spin $j_b = J - s_Q$), become "good" quantum numbers. Then, the heavy-quark spin doublet states are formed, which are degenerated in the heavy quark limit. These behaviors of baryons characterized by heavy quarks should be reflected in the level structure, the production rates, and the decay properties. Through spectroscopic investigations of excited baryons, we could learn the nature of baryons over various flavors with respect to the quark masses.

We demonstrate how the level structure of baryons behaves as the quark masses. Fig. 26 shows a level scheme of the excitation energies in the cases of Λ baryons as

a function of the heavy quark mass (m_Q), where a Λ baryon can be described as a system of a single heavy quark and the two light quarks, Qqq, with the isospin equal to zero. Lines are calculated by a non-relativistic quark model [45] as changing m_Q, each of which shows the average of the spin-orbit splitting states. They are good guide lines to see relations between excited states with the same spin-parity over the various flavors. One finds that some of lines are closer as m_Q becomes larger, which are due to the heavy quark symmetry in the spin-spin interaction, as is the case of the heavy quark spin doublet formed by the spin-orbit interaction. Through these behaviors, we could learn how internal structures of excited states as the quark mass changes.

Now let us turn to the systems of ssQ, Ω_Q baryons. In Fig. 27, we draw 5 lines for excited S- and P-states, connecting the states with having the same spatial (parity) and spin configuration but different masses (flavors). Excitation energies for Ξ, Ω, Ω_c, and Ω_b reported by the Partice Data Group (PDG) [1] are overlaid for reference. Most of their quantum numbers have not been determined. From this figure, we observe that unique features are the degeneracy of the λ and ρ modes (the point of the upper circle at $Q = s$), and forbidden modes at $Q = s$ due to the Pauli exclusion principle (crosses at $Q = s$). These observations are not yet established experimentally that can be primarily studied in the K10 project. In addition, there is furthe unique features in the ssQ Ω_Q baryons as we discuss in the next subsection.

A.2 Baryon with a single heavy quarks with two-strange quarks

The systems ssQ with no u, d quarks that we have discussed so far are considered very different from the protons and neutrons, where pion clouds surround the nucleon forming the tail of the structure. Hence we have a picture for the nucleon, the quark core and the pion cloud around it. The pion of light mass is the necessity of spontaneous symmetry breaking of chiral symmetry and leads to various model independent relations as the low energy theorems. The pion also gives the most important component of the nuclear force at long distances. In spite of these good features, the pion may complicate the structure of the nucleon and makes it difficult to establish a unified description including its resonances. Moreover, the light pions are easily emitted from the resonances, that makes theoretical analysis involved.

In the standard quark model where the pion cloud is not taken into account, baryons are qqq and their resonances are described as single particle excitations of the constituent quarks. In this word, the quark model explains properties of many low lying hadrons qualitatively with various flavors including heavy quarks. It also describes the short range part of the nuclear force which has been supported by the recent lattice calculations. A very opposite description of the nucleon emerges when maximally utilizing the pion cloud. This is the skyrmion for the nucleon. In this picture the nucleon excitations emerge as collective motion of the pionic soliton. The model is good at describing the phenomena where the pion is involved. The nucleons or in general hadrons containing light quarks share both features quark dynamics and pion dynamics in some way or another.

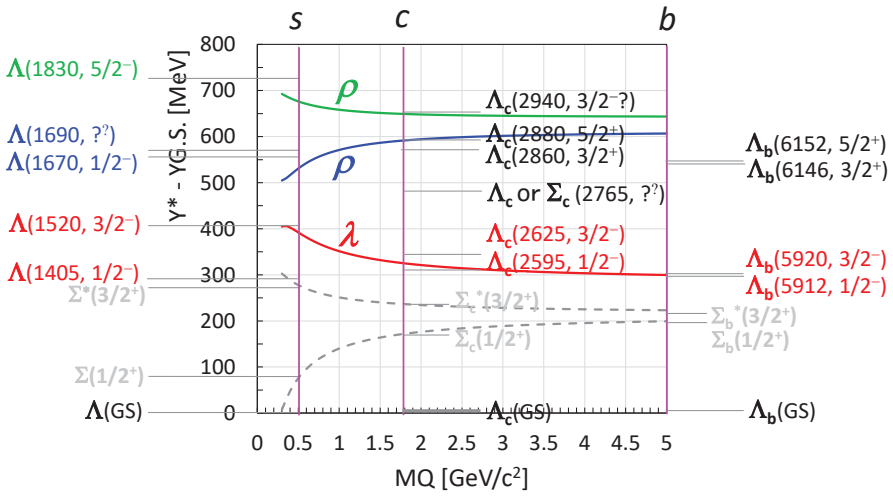

Figure 26: Excitation energy scheme in the cases of Λ_Q baryons based on a constituent quark model

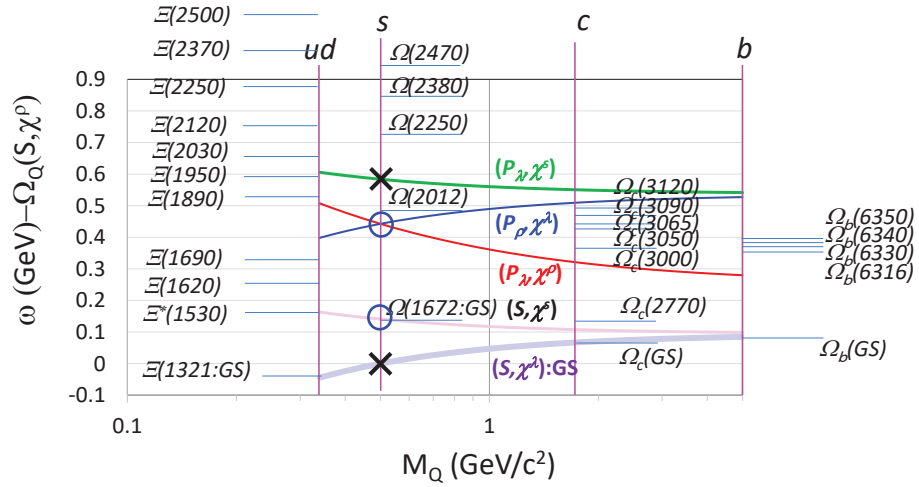

Figure 27: Excitation energy scheme in the cases of Ω_Q baryons

The two models reflect important aspects of QCD, but their advantages are somewhat different. In some cases they make very different predictions. Under such situation, we propose to explore the study of baryons removing pion clouds, "pionless spectroscopy". This should be useful to unveil the genuine role of the constituent quarks, and in turn that of the pions. Our eventual goal is then to establish an effective method keeping its applicability to explain and predicts various hadron phenomena.

A.3 Determination of spin and parity

In Fig. 28, arrows indicate decay schemes of the excited Ω's. Solid arrows indicate observed channels in PDG and dashed ones are to be observed. The excited states of Ω are expected to decay into a low-lying Ξ state associated with an anti-kaon emission mainly, as the pion emissions are suppressed. The determination of the spin of the initial baryons can be performed by the measurement of angular distribution of decaying particle. The expected angular distribution in the $\Omega^*(J^P) \to \bar{K}(0^-)\Xi(1/2^+)$ decay is expressed as

$$\begin{array}{lll} W(\theta) \propto & 1 & \text{for } J = 1/2, \\ W(\theta) \propto & 3\rho_{33}\sin^2\theta + \rho_{11}(1 + 3\cos^2\theta) & \text{for } J = 3/2, \text{and} \\ W(\theta) \propto & 5\rho_{55}(1 - \cos^2\theta)^2 + \rho_{33}(1 + 14\cos^2\theta - 15\cos^4\theta) & \\ & +2\rho_{11}(1 - 2\cos^2\theta + 5\cos^4\theta) & \text{for } J = 5/2. \end{array} \tag{14}$$

Here, we ignore the off-diagonal elements of the spin-density matrix elements $\rho_{2J2J'}$. The polar angle θ and azimuthal angle ϕ is given by the direction of flight of Ξ^0 (one of the daughter particles) in the rest frame of Ω^*. The z-axis is defined to be opposite to the K^+K^{*0} composite system. The off-diagonal terms vanish for the decay angular distribution when it is integrated over ϕ. Another method can be considered to determine the spin of Ω^* together with its parity when we find the sequential reaction $K^-p \to \Xi^{*0}K^{*0}$ followed by $\Xi^{*0} \to \Omega^{*-}K^+$. As shown in Fig. 29, the excited Ξ state may decay into Ω^* and K^+. In this case, the spin-parity of the Ω^* state can be determined by the angular correlation between K^{*0} and K^+,

To determine the parity, we may use the relative orbital angular momentum value λ of the two-body decaying particles. For instance in the decay process of $1/2^- \to 1/2^+ + 0^-$, the relative angular momentum of the decaying particles is S-wave, while the decay of $1/2^+ \to 1/2^+ + 0^-$ occurs in the P-wave. Because the decay width is proportional to $p^{2\lambda+1}$, for a typical value of a few hundred MeV of p the decays into two particles of higher partial wave are suppressed as compared to those of lower partial waves. Here p is the relative momentum of the decaying two particles, and the suppression is caused by the power of the combination p/Λ where $\Lambda \sim 0.8$ GeV is the inverse of a typical hadron size ~ 0.5 fm.

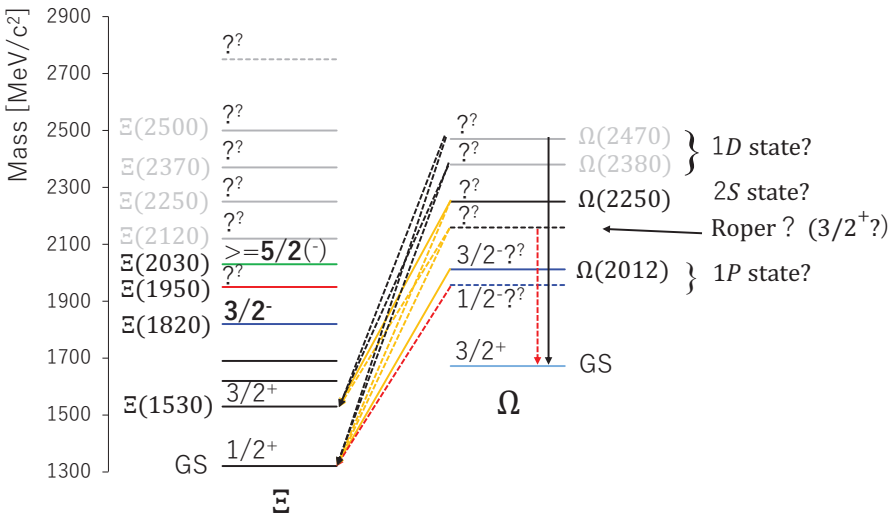

Figure 28: Level scheme of Ω and Ξ baryons. Observed (solid arrows) and expected (dashed arrows) decay channels are shown.

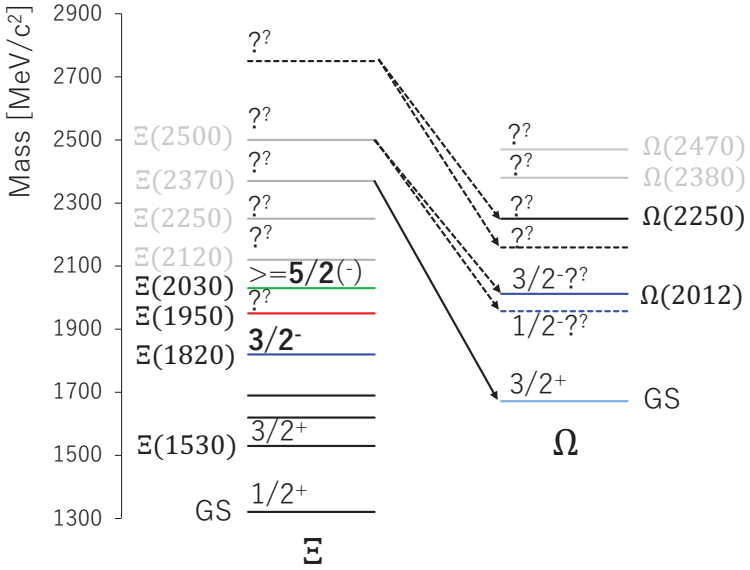

Figure 29: Expected production schemes of excited Ω baryons via the excited Ξ baryons associated with a kaon emission.

B ΩN scattering

B.1 Introduction

In addition to the Ω^*-mass spectrum, scattering of the ground-state Ω^- on the nucleon N is of fundamental importance to be studied. The $\Omega^- N$ system belongs to the octet as well as ΔN with $J = 2$ among the decuplet-baryon and octet-baryon systems:

$$10 \otimes 8 = 35 \oplus 8 \oplus 10 \oplus 27. \tag{15}$$

Recently, a lattice QCD calculation predicts an bound state in the ΩN system owing to absence of a repulsive core in its ${}^5S_2$ state, and its weak absorption to another channel.

Currently, the low-energy ΩN scattering is studied using the momentum correlation function of the $\Omega^- p$ pairs in relativistic heavy-ion collisions (so called the femtoscopy) [46]. The function shows a depletion below 1 around 20–40 MeV corresponding to attraction with a positive scattering length, suggesting a shallow bound state. The existence of an $\Omega^- p$ bound state cannot be concluded since information on the $J = 1$ $\Omega^- p$ potential is not sufficient. Therefore, desired is a direct ΩN scattering experiment, and it can be realized at the K10 beam line thanks to a rather stable nature of Ω^- (only it decays in the weak interaction).

B.2 Production of the ΩN bound state

An experiment should be conducted for measuring the low-energy ΩN scattering cross section, and/or for determining the mass and width of the possible ΩN bound state. The two reactions are considered for these purposes here:

1. Ω^- is produced by the $K^- d \to \Omega^- K^+ K^{(*)0} n$ reaction in a deuteron, followed by the $\Omega^- n$ reaction in another deuteron ($\Omega^- d$ scattering), and

2. $\Omega^- n$ is directly produced by the $K^- d \to \Omega^- n K^+ K^{(*)0}$ reaction in a deuteron (direct $\Omega^- N$ production).

Figure 30 shows the diagrams of these reactions for producing the low-energy ΩN system including the ΩN bound state. In $\Omega^- d$ scattering, we select the $\Omega^- n \to \Xi^- \Lambda$ events by detecting the final-state $p\pi^-$ particles from the Λ decay and $p\pi^-\pi^-$ from $\Xi^- \to \Lambda\pi^-$ followed by $\Lambda \to p\pi^-$. It should be noted that a finite distance is observed in this case between the production vertex of Ω^- and decay (or scattering) vertex of $\Omega N \to \Xi^- \Lambda$. In direct $\Omega^- N$ production, we measure the final-state $K^+ K^{(*)0}$ particles for ΩN production, and the $\Xi^- \Lambda$ for the ΩN decay. The analysis procedure is very similar to that for $\Omega^- d$ scattering but the production vertex of Ω^- and decay vertex of $\Omega N \to \Xi^- \Lambda$ is common in direct $\Omega^- N$ production. The total number of emitted particles is 8 in the events to be analyzed.

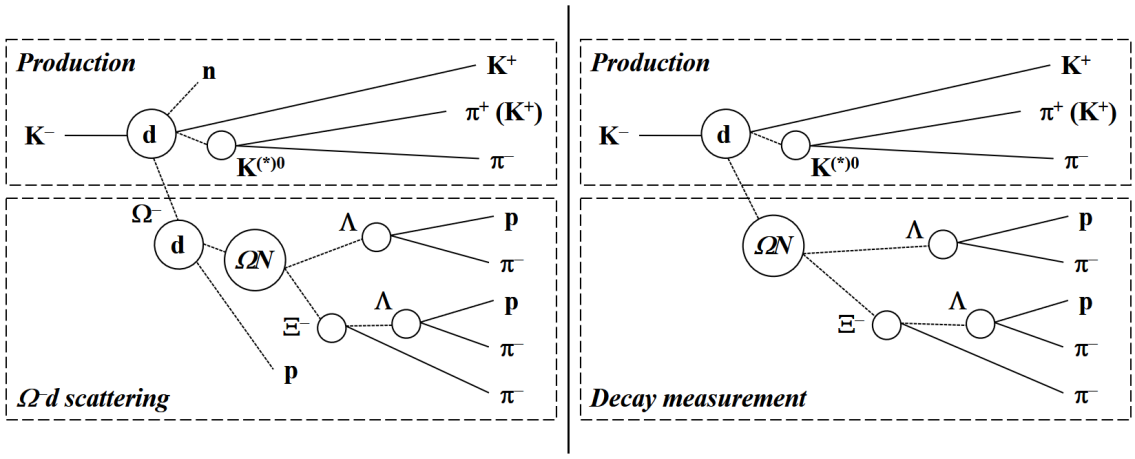

Figure 30: Diagrams for producing the low-energy ΩN system including the ΩN bound state. (a) Ω^- is produced by the $K^- d \to \Omega^- K^+ K^{(*)0} n$ reaction in a deuteron, followed by the $\Omega^- n$ reaction in another deuteron ($\Omega^- d$ scattering). (b) the $\Omega^- n$ system is directly produced by the $K^- d \to \Omega^- n K^+ K^{(*)0}$ reaction in a deuteron (direct $\Omega^- N$ production). The solid lines represent the initial- and final-state particles to be directly detected. The dashed lines show unstable particles to be reconstructed from kinematic variables of the detected particles, and spectator nucleons difficult to be detected.

B.3 Requirements for the spectrometer

To produce the low-energy ΩN system, we need high-intensity high-momentum negative-kaon beam similarly to Ω^* production. At such incident kaon momenta, almost all the particles are likely to be emitted at forward angles in the laboratory frame. A spectrometer system with a dipole magnet covering the forward direction is also suitable to detect the final-state particles in ΩN production. The requirements of the spectrometer for the experiment producing Ω^*s is common to ΩN production. However, the number of the final-state particles to be detected in ΩN production is larger than that in Ω^* production. Additional items should be considered as follows:

- the target is located inside the gap of the dipole magnet for maximizing the acceptance of the multiple particle detection with a wide angular coverage,
- additional detectors are required for surrounding the target for effectively detecting daughter π^-s from the $\Omega^- n$ decay emitted at backward angles up to $\sim 90°$ with a momentum lower than 1 GeV/c,
- the amount of substance in the additional detectors should be small to avoid the multiple scattering and nuclear reactions of the slow πs,
- precise vertex determination is required for recognizing finite flight lengths of Ω^-, Ξ^-, and Λ by detecting the daughter particles from rather stable Ξ^- and Λ

particles for reducing a combinatorial background,

- the momentum resolution (Δp/p) is better than 0.2%(σ) to achieve enough ΩN-mass resolution of $\sim$ 1 MeV(σ) (comparable or better than the $\Omega^- n$ width, and
- large acceptance as long as possible and high momentum-resolution of a few $10^{-3}(\sigma)$ for the other high-momentum final-state $K^+K^+\pi^-$ ($K^+\pi^+\pi^-$) emitted at forward angles to give an $S = -3$ condition.

Required are additional detectors surrounding the target to detect slow daughter π^-s from the $\Omega^- n$ decay with a wide angular coverage.

B.4 Yield for the ΩN bound state

As already discussed, we select the $\Omega^- n \to \Xi^-\Lambda$ events by detecting the final-state $p\pi^-$ particles from the Λ decay and $p\pi^-\pi^-$ from $\Xi^- \to \Lambda\pi^-$ followed by $\Lambda \to p\pi^-$ both in $\Omega^- d$ scattering and direct $\Omega^- N$ production. A difference of two reactions are observed in the distance between the production vertex of Ω^- and decay vertex of $\Omega N \to \Xi^-\Lambda$. It is crucial to confirm each decay vertex of $K^{(*)0}$, Ξ^-, and Λ is consistent with a composite three-momentum and previous decay (or production) vertex for reducing the combinatorial background.

We estimate the ΩN-mass spectrum in the direct ΩN-production case at an incident kaon momentum of 7 GeV/c in a similar simulation using the E50 spectrometer to Ω^* production. Here, it is assumed that the possible $\Omega^- n$ bound state takes a Breit-Wigner shape, and that its mass and width is 2611 and 1.4 MeV, respectively, Both the angular distribution assumed is isotropic in the CM frame for ΩN production and in the rest frame of ΩN for the decay. The acceptance estimated is $\sim$ 25% for detecting $K^+K^{(*)0}$ associated with ΩN production, and that is $\sim$ 42% for detecting $\Xi^-\Lambda$ in the ΩN decay. Therefore, the acceptance is $\sim$10% for detecting all the particles from $K^+K^{(*)0}$ and $\Xi^-\Lambda$. Figure 31 shows the momentum distributions of the final-state K^+, p and π^- particles, and correlations between the emission angle and momentum for them. K^+s and π^-s are distributed in a wide angular range, and those emitted at backward angles ($\theta_{\rm LAB} > 40^\circ$) are not detected with the E50 spectrometer. The E50 spectrometer is not suitable for the study of the possible ΩN bound state since the spectrometer does not cover backward angles. Desired is construction of a new spectrometer dedicated to this study with additional detectors surrounding the target to increase the acceptance for the final-state particles emitted at backward angles. In the yield estimation, it is assumed that both the acceptances are 80% using a dedicated new spectrometer for detecting $K^+K^{(*)0}$ and for detecting $\Xi^-\Lambda$.

The yield is estimated for the events that the $\Omega^- n$ bound state is produced at the incident beam momentum of 7 GeV/c. The number of the Ω^--produced is 10.0 and 0.48 in a spill in the $K^-\ p \to \Omega^-\ K^+\ K^0$ and $K^-\ p \to \Omega^-\ K^+\ K^{*0}$ reactions with cross sections of 2.0 and 0.05 μb, respectively. Once the produced Ω^-s are identified, they can be used as incident particles with an intensity of 10.5/spill to produce the

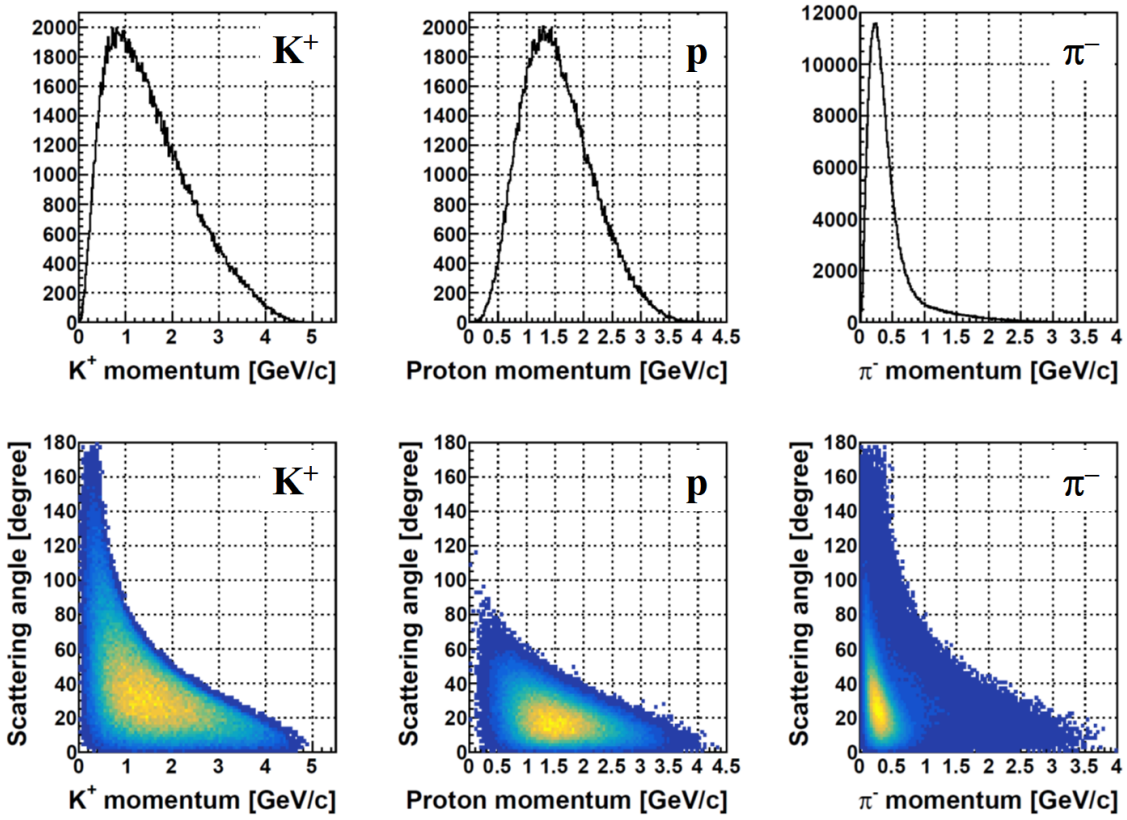

Figure 31: Momentum distributions of the final-state K^+, p and π^- particles from the left to right panels (top). Correlation plots between the emission angle and momentum for K^+, p and π^- from the left to right panels (bottom).

$\Omega^- n$ bound state. The total cross section assumed is 3.6 mb for the $\Omega^- n$ reaction. The branching ratio (fraction) of $\Omega^- n \to \Xi^- \Lambda$ assumed is 0.80. The average flight length of the produced Ω^-s is $\beta\gamma c\tau \sim 5.2$ cm at an incident kaon momentum of 7 GeV/c since their average momentum is 3.5 GeV/c. Thus, the effective mass-thickness of the deuteron target is 0.8 g/cm^2. The total efficiency is 0.50 for five-track events where the in-flight decay of π^-s is not considered. The production rate is found to be $\sim$ 20 a day for the events that the $\Omega^- n$ bound state is produced. We can detect $\sim$2000 events in a 100-day beam time. Additional factors are listed in Table 7 for estimating the yield for the events that the $\Omega^- n$ bound state is produced. In this estimation, direct $\Omega^- n$ production is not included. If this cross section is $\sim$0.3 nb, the yield of $\sim$1000 can be additionally obtained.

Table 7: Different factors from Table 3 for estimating the $\Omega^- d$-scattering events at the incident beam momentum of 7 GeV/c.

Reaction	$K^- p \to \Omega^{*-} K^+ K^0$	$K^- p \to \Omega^{*-} K^+ K^{*0}$
Cross section	2.0 μb	0.05 μb
Acceptance	0.80	0.80
Ω^- rate in a spill	10.0	0.48
Total Ω^- rate in a spill	10.5	
Cross section (ΩN scattering)	3.6 mb	
Branching ratio ($\Omega N \to \Xi^- \Lambda$)	0.80	
Branching ratio($\Lambda \to p \pi^-$)	0.64	
branching ratio ($\Xi \to \Lambda \pi^-$)	0.99	
Average Ω^- flight length	5.2 cm	
Effective target thickness	0.8 g/cm^2	
Acceptance ($\Omega N \to \Xi^- \Lambda$)	0.80	
Total efficiency	0.50 (five-track events)	
Expected yield in a 100-day beam time	2.0×10^3	

B.5 Mass resolution for the ΩN bound state

The $\Omega^- n$-mass resolution is estimated assuming the $\Omega^- n$ is determined by the $\Xi^-\Lambda$ invariant mass with a momentum resolution of $\Delta p_{\rm spec}/p_{\rm spec} = 0.2\%(\sigma)$ for the final-state particles. Figure 32 shows the $\Xi^-\Lambda$ invariant-mass spectrum for the $\Omega^- n$ bound state. Here, 10^4 events are generated for the $\Omega^- n$ bound state. The combinatorial background coming from the wrong combinations of the final-state particles for reconstructing unstable particles. The mass resolution estimated for the $\Omega^- n$ state is ~ 1 MeV (σ) when the momentum resolution is $\Delta p_{\rm spec}/p_{\rm spec} = 0.2\%(\sigma)$ for the final-state particles. The width of the mass spectrum becomes 1.6 MeV(σ) by incorporating the 1.4-MeV width of the $\Omega^- n$ bound state.

The straggling effects of the energy loss in the target material also deteriorate the $\Omega^- n$-mass resolution. Figure 33 shows the $\Xi^-\Lambda$ invariant-mass spectra for 2000 events of the $\Omega^- n$ bound state with different straggling effects and different momentum resolution. Plotted are the spectra with a width of 0 and 1.4 MeV for the $\Omega^- n$ bound state. The momentum resolution is required to be better than $\Delta p_{\rm spec}/p_{\rm spec} = 0.2\%(\sigma)$ for the final-state particles to recognize the broadening of the $\Omega^- n$ peak owing to the width of the $\Omega^- n$ bound state. The straggling effect of 1 MeV (σ) of the energy loss makes the broadening of the $\Omega^- n$ peak by the momentum resolution of $\Delta p_{\rm spec}/p_{\rm spec} = 0.2\%(\sigma)$ is equivalent to that by the $\Omega^- n$ width of 1.4 MeV. The broadening of the $\Omega^- n$ peak can be observed owing to the width of the $\Omega^- n$ bound state even if the straggling effect is 1 MeV(σ.) of the energy loss. It is difficult to determine the width

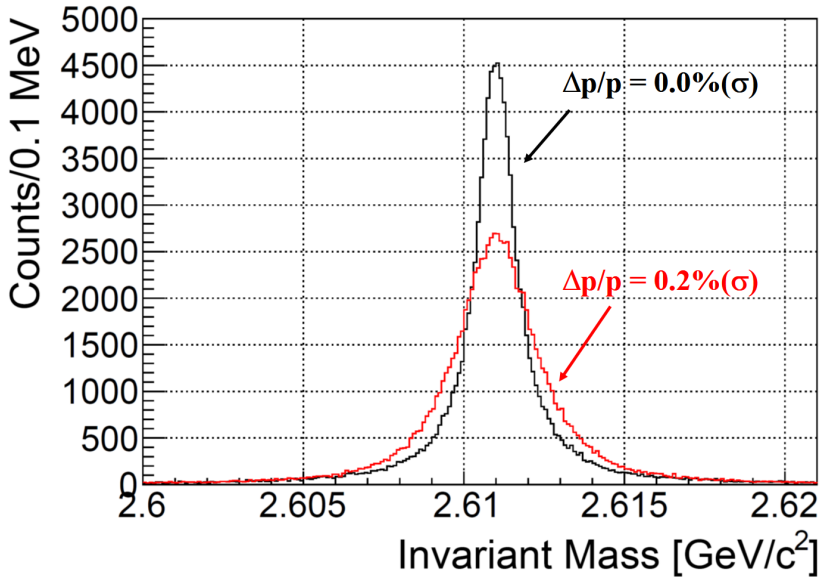

Figure 32: $\Xi^-\Lambda$ invariant-mass spectrum for the $\Omega^- n$ bound state. The black curve corresponds to the spectrum for the expected $\Omega^- n$ bound state, and the red one shows that with incorporating the experimental mass resolution.

of the $\Omega^- n$ bound state if the straggling effect becomes 2 MeV(σ.) of the energy loss. The straggling effect should be lowered less than 1 MeV(σ).

By fitting a Breit-Wigner function convoluted by a Gaussian to the $\Omega^- n$-spectra shown in Fig. 33, the measured widths for the $\Omega^- n$ bound state are estimated for different straggling effects of the energy loss, and different momentum resolutions for the final-state particles. Figure 34 shows the measured width for the $\Omega^- n$ bound state as a function of the straggling effect of the energy loss. Required are high momentum-resolution better than $\Delta p_{\rm spec}/p_{\rm spec} = 0.2\%$ (σ) and small straggling effect of the energy loss less than 1 MeV(σ). When the momentum resolution is $\Delta p_{\rm spec}/p_{\rm spec} = 0.2\%$ and the straggling effect of the energy loss is 1 MeV(σ), the accuracy of the width determination is found to be $\pm$0.1 MeV (σ).

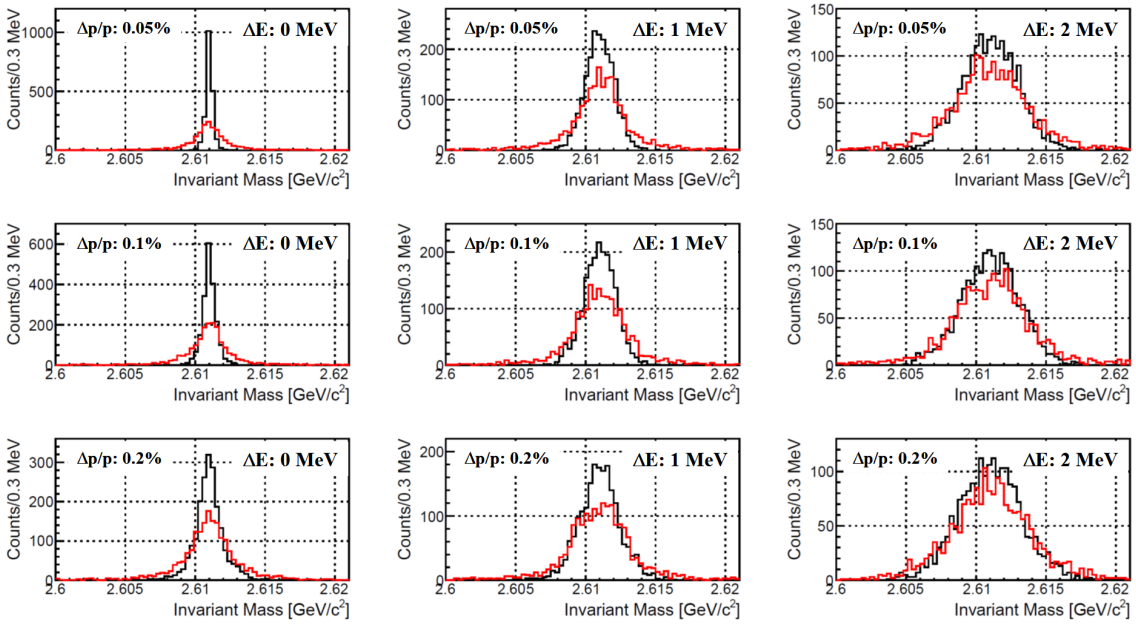

Figure 33: $\Xi^-\Lambda$ invariant-mass spectra for 2000 events of the $\Omega^- n$ bound state with different momentum resolution ($\Delta p_{\rm spec}/p_{\rm spec}$ = 0.05, 0.1, and 0.2% (σ) from the top to the bottom) and different straggling effects of the energy loss in the target material (0, 1, and 2 MeV(σ) from the left to the right). In each panel, the black curve shows the measured spectrum for the ΩN bound state with a width of 0, and the red for the state taking a Breit-Wigner shape with a width of 1.4 MeV.

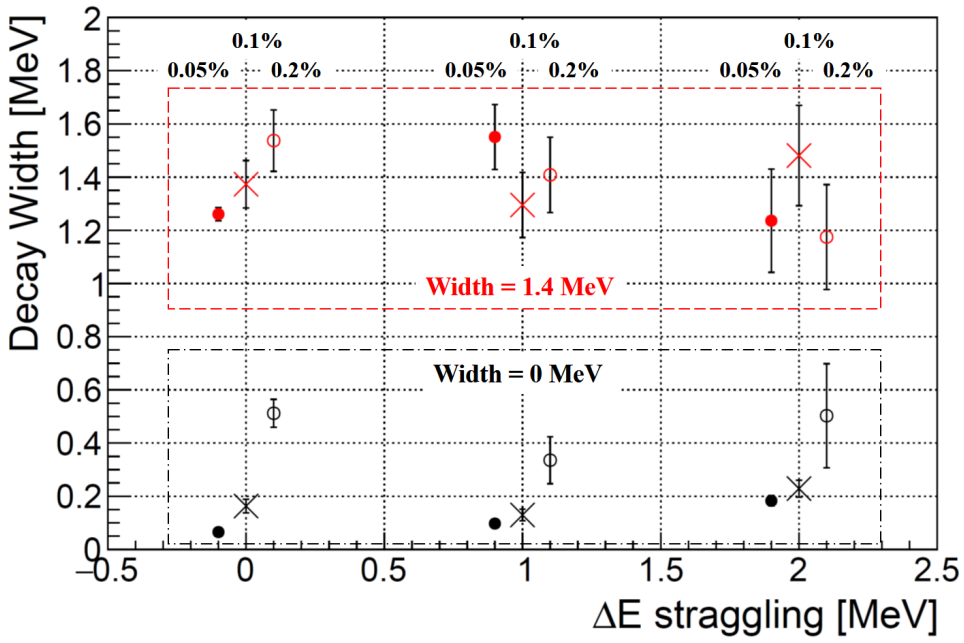

Figure 34: Measured width for the $\Omega^- n$ bound state as a function of the straggling effect of the energy loss in the target material (0, 1, and 2 MeV (σ)). The filled circles, X markers, and open circles represent the data for $\Delta p_{\rm spec}/p_{\rm spec}$ = 0.05%, 0.1%, and 0.2% (σ), respectively. The black and red makers represent the data for the state with widths of 0 and 1.4 MeV.

C ES-separator option for K10 beamline

The layout of the ES-separator option of the K10 beam line is presented in Fig.35, and the beam envelope calculated with the TRANSPORT code is shown in Fig.36. The total length of the beam line is 82.8 m, which is almost same as that of the RF option.

The front-end section from the production target to the IF is completely same as that in the RF option. The separation of the secondary particles is performed by using three ES separators. Each of the ES separators have the effective length of 9 m, the electrode gap of 10 cm, and the electrostatic field of 75 kV/cm. In the separation section, parallel beams are made in both the horizontal and vertical directions to pass through such long ES separators, and then the beams are focused vertically at the mass slit (MS). They are analyzed with the beam spectrometer in the analyzing section, and finally focused both horizontally and vertically at an experimental target. In addition, there are two horizontal focal points in the beam line (HF1, HF2), where slits are located to determine the momentum bite and to increase the beam purity.

The beam intensity and purity of the beam line was estimated by using a lay-tracing code DecayTURTLE. The assumption for the beam loss and spill repetition is same as that for the RF option. The result is summarized in Table 8.

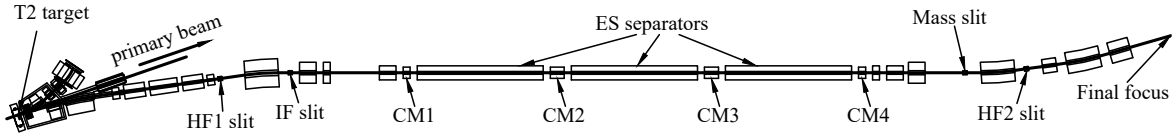

Figure 35: Layout of the ES option of the K10 beam line.

Table 8: The expected intensity and purity of the ES option of the K10 beam line. Assumed condition of the primary protons is same as Table 2.

	4 GeV/c K^-	4 GeV/c $\bar{p}$	6 GeV/c $\bar{p}$
acceptance [msr-%]	0.33	1.2	0.55
intensity [/spill]	1.6×10^6	1.5×10^7	7.5×10^6
purity ($K^- : \pi^-$ or $\bar{p} : \pi^-$)	1.1:1	81:1	1:3.4

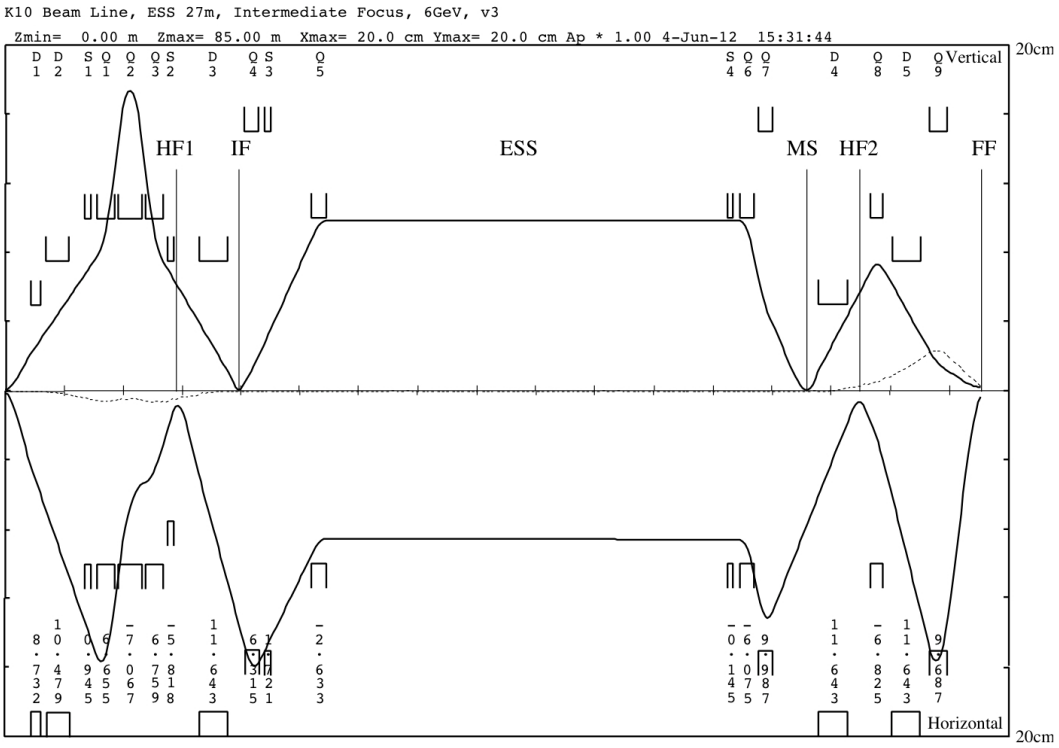

Figure 36: First-order beam envelope of the ES option of the K10 beam line. The upper and lower show the vertical and horizontal directions, respectively. The dash line indicate the horizontal dispersion.

References

[1] **Particle Data Group** Collaboration, P. Zyla *et al.*, "Review of Particle Physics," *PTEP* **2020** no. 8, (2020) 083C01.

[2] M. Takayama, H. Toki, and A. Hosaka, "Systematics of the SU(3) baryon spectra and deformed oscillator quark model," *Prog. Theor. Phys.* **101** (1999) 1271–1283.

[3] G. 't Hooft, "How Instantons Solve the U(1) Problem," *Phys. Rept.* **142** (1986) 357–387.

[4] G. 't Hooft, "Symmetry Breaking Through Bell-Jackiw Anomalies," *Phys. Rev. Lett.* **37** (1976) 8–11.

[5] G. 't Hooft, "Computation of the Quantum Effects Due to a Four-Dimensional Pseudoparticle," *Phys. Rev. D* **14** (1976) 3432–3450. [Erratum: Phys.Rev.D 18, 2199 (1978)].

[6] A. Manohar and H. Georgi, "Chiral Quarks and the Nonrelativistic Quark Model," *Nucl. Phys. B* **234** (1984) 189–212.

[7] M. Gell-Mann, "A Schematic Model of Baryons and Mesons," *Phys.Lett.* **8** (1964) 214–215.

[8] L. W. Alvarez, "Certification of three old cosmic ray emulsion events as omega-decays and interactions," *Phys. Rev. D* **8** (1973) 702–711.

[9] V. E. Barnes *et al.*, "Observation of a Hyperon with Strangeness Minus Three," *Phys. Rev. Lett.* **12** (1964) 204–206.

[10] S. Takeuchi, "Spin orbit force of instanton induced interaction in strange and charmed systems," *Nucl. Phys. A* **642** (1998) 543–561, `arXiv:hep-ph/9807240`.

[11] T. Yoshida, E. Hiyama, A. Hosaka, M. Oka, and K. Sadato, "Spectrum of heavy baryons in the quark model," *Phys. Rev. D* **92** no. 11, (2015) 114029, `arXiv:1510.01067 [hep-ph]`.

[12] **Belle** Collaboration, J. Yelton *et al.*, "Observation of an Excited Ω^- Baryon," *Phys. Rev. Lett.* **121** no. 5, (2018) 052003, `arXiv:1805.09384 [hep-ex]`.

[13] M.-S. Liu, K.-L. Wang, Q.-F. Lü, and X.-H. Zhong, "Ω baryon spectrum and their decays in a constituent quark model," *Phys. Rev. D* **101** no. 1, (2020) 016002, `arXiv:1910.10322 [hep-ph]`.

[14] M. P. Valderrama, "$\Omega(2012)$ as a hadronic molecule," *Phys. Rev. D* **98** no. 5, (2018) 054009, `arXiv:1807.00718 [hep-ph]`.

[15] N. Ikeno, G. Toledo, and E. Oset, "Molecular picture for the $\Omega(2012)$ revisited," *Phys. Rev. D* **101** no. 9, (2020) 094016, arXiv:2003.07580 [hep-ph].

[16] **Belle** Collaboration, T. J. Moon *et al.*, "First Determination of the Spin and Parity of a Charmed-Strange Baryon, $\Xi_c(2970)^+$," arXiv:2007.14700 [hep-ex].

[17] **CMS** Collaboration, A. M. Sirunyan *et al.*, "Study of excited Λ_b^0 states decaying to $\Lambda_b^0\pi^+\pi^-$ in proton-proton collisions at $\sqrt{s} = 13$ TeV," *Phys. Lett. B* **803** (2020) 135345, arXiv:2001.06533 [hep-ex].

[18] **LHCb** Collaboration, R. Aaij *et al.*, "Observation of a new baryon state in the $\Lambda_b^0\pi^+\pi^-$ mass spectrum," *JHEP* **06** (2020) 136, arXiv:2002.05112 [hep-ex].

[19] N. Suzuki, B. Julia-Diaz, H. Kamano, T. S. H. Lee, A. Matsuyama, and T. Sato, "Disentangling the Dynamical Origin of P-11 Nucleon Resonances," *Phys. Rev. Lett.* **104** (2010) 042302, arXiv:0909.1356 [nucl-th].

[20] V. D. Burkert and C. D. Roberts, "Colloquium : Roper resonance: Toward a solution to the fifty year puzzle," *Rev. Mod. Phys.* **91** no. 1, (2019) 011003, arXiv:1710.02549 [nucl-ex].

[21] S. Weinberg, "Why do quarks behave like bare Dirac particles?," *Phys. Rev. Lett.* **65** (1990) 1181–1183.

[22] T. Kubota and K. Ohta, "Relativistic Corrections to the Baryon Resonance Photoexcitation Amplitudes in the Quark Model," *Phys. Lett. B* **65** (1976) 374–376.

[23] A. J. Arifi, D. Suenaga, and A. Hosaka, "Relativistic corrections to decays of heavy baryons in the quark model," *Phys. Rev. D* **103** no. 9, (2021) 094003, arXiv:2102.03754 [hep-ph].

[24] B. Julia-Diaz, D. O. Riska, and F. Coester, "Axial transition form-factors and pion decay of baryon resonances," *Phys. Rev. C* **70** (2004) 045204, arXiv:nucl-th/0406015.

[25] J. Sanford and C. Wang *BNL internal reports* **No.11299 and 11479** (1962) .

[26] http://aea.web.psi.ch/Urs_Rohrer/MyWeb/trans.htm .

[27] http://aea.web.psi.ch/Urs_Rohrer/MyWeb/turtle.htm .

[28] H. Noumi *et al. KEK/J-PARC-PAC 2012-19* **2012-19** (2012) .

[29] K. Shirotori, "Spectrometer for the charmed baryon spectroscopy experiment at the J-PARC high-momentum beam line," *PoS* **Hadron2013** (2013) 130.

[30] T. Aramaki *et al.*, "Performance evaluation of a scintillating fiber detector for the high-momentum secondary beamline at J-PARC," *ELPH annual report, Tohoku University* **2018** (2019) 44.

[31] T. Akaishi *et al.*, "Development of a beam-timing detector for the charmed-baryon spectroscopy experiment at J-PARC," *ELPH annual report, Tohoku University* **2018** (2019) 58.

[32] M. Naruki *et al.*, "Development of RICH detector for Secondary Beam Particles at J-PARC High-momentum Beamline," *RCNP annual report, Osaka University* **2020** (2020) .

[33] R. Honda *et al.*, "Continuous timing measurement using data streaming DAQ system based on FairMQ," *paper in preparation* .

[34] Y. Ma *et al.*, "Performance evaluation of the next generation DAQ system with high-rate detectors for the J-PARC E50 experiment," *ELPH annual report, Tohoku University* **2018** (2019) .

[35] T. Ishikawa *et al.*, "The second GeV tagged photon beamline at ELPH," *Nucl. Instrum. Meth. A* **622** (2010) 1–10.

[36] **Amsterdam-CERN-Nijmegen-Oxford** Collaboration, S. N. Ganguli *et al.*, "A Study of Inclusive Ξ^- Production from K- p Interaction at 4.2-GeV/c," *Nucl. Phys. B* **128** (1977) 408–420.

[37] **Amsterdam-CERN-Nijmegen-Oxford** Collaboration, R. J. Hemingway *et al.*, "Ω^- Produced in K^-p Reactions at 4.2-GeV/c," *Nucl. Phys. B* **142** (1978) 205–219.

[38] J. K. Hassall, R. E. Ansorge, J. R. Carter, W. W. Neale, J. G. Rushbrooke, D. R. Ward, B. Y. Oh, M. Pratap, G. A. Smith, and J. Whitmore, "Production of S = -2 and -3 Baryon States in 6.5-GeV/cK^-P Interactions," *Nucl. Phys. B* **189** (1981) 397–420.

[39] **Birmingham-CERN-Glasgow-Michigan State-Paris** Collaboration, M. Baubillier *et al.*, "A Study of Inclusive Xi-, Xi (1530) and ω^- Production in K^-p Interactions at 8.25-GeV/c," *Nucl. Phys. B* **192** (1981) 1–17.

[40] **Aachen-Berlin-CERN-London-Vienna** Collaboration, P. Sixel *et al.*, "INCLUSIVE PRODUCTION OF XI- AND XI* (1530) IN K- p INTERACTIONS AT 10-GeV/c AND 16-GeV/c," *Nucl. Phys. B* **159** (1979) 125.

[41] D. Aston *et al.*, "Inclusive Production of Multistrange Hyperons From 11-GeV/c K^-p Interactions," *Phys. Rev. D* **32** (1985) 2270.

[42] Y. Nara, N. Otuka, A. Ohnishi, K. Niita, and S. Chiba, "Study of relativistic nuclear collisions at AGS energies from p + Be to Au + Au with hadronic cascade model," *Phys. Rev. C* **61** (2000) 024901, arXiv:nucl-th/9904059.

[43] B. Andersson, G. Gustafson, G. Ingelman, and T. Sjostrand, "Parton Fragmentation and String Dynamics," *Phys. Rept.* **97** (1983) 31–145.

[44] T. Sjostrand, S. Mrenna, and P. Z. Skands, "A Brief Introduction to PYTHIA 8.1" *Comput. Phys. Commun.* **178** (2008) 852–867, arXiv:0710.3820 [hep-ph].

[45] T. Yoshida, E. Hiyama, A. Hosaka, M. Oka, and K. Sadato, "Spectrum of heavy baryons in the quark model," *Phys. Rev. D* **92** no. 11, (2015) 114029, arXiv:1510.01067 [hep-ph].

[46] K. Morita, S. Gongyo, T. Hatsuda, T. Hyodo, Y. Kamiya, and A. Ohnishi, "Probing $\Omega\Omega$ and $p\Omega$ dibaryons with femtoscopic correlations in relativistic heavy-ion collisions," *Phys. Rev. C* **101** no. 1, (2020) 015201, arXiv:1908.05414 [nucl-th].